공 학 박 사 학 위 논 문

Development of Hybrid Electrochemical Water Treatment System Combined of Deionization and Oxidation

탈염과 산화를 결합한 하이브리드
전기화학적 수처리 시스템 개발

2017년 2월

서울대학교 대학원

화학생물공학부

김 성 환

Development of Hybrid Electrochemical Water Treatment System Combined of Deionization and Oxidation

by

Seonghwan Kim

under the supervision of

Professor Jeyong Yoon, Ph. D.

A dissertation submitted in partial fulfillment of the requirements for the Degree of
Doctor of Philosophy

February 2017

SCHOOL OF CHEMICAL AND BIOLOGICAL ENGINEERING
SEOUL NATIONAL UNIVERSITY

Abstract

Over recent decades, the lack of available water has been considered as a critical challenge for mankind. Electrochemical water treatment can be a promising alternative due to its high energy efficiency, eco-friendliness and lack of required hazardous chemicals. Capacitive deionization (CDI), electrodialysis (ED) and desalination battery are well-established demonstrations that are successfully converged of materials used for energy storage with electrochemical system for water treatment. These demonstrations accomplish electrochemical deionization by means of the operational principle of energy storage in energy storage systems (e.g., supercapacitors and batteries). Although they provide an energy efficient deionization process, the systems have suffered from the limitations in their systems and materials, attributing to difficulties to find suitable compounds/systems for capturing anions and retain the stability of active material in aqueous system.

In this dissertation, it is demonstrated that a novel electrochemical water treatment system combined of deionization and oxidation, and suitable materials for intercalation/deintercalation of cations. First of all, a novel

hybrid electrochemical water treatment system consisting of an electrochemical desalination system synchronized with an oxidation process is developed. The hybrid electrochemical water treatment system consists of electrode material for the sodium ion battery as a desalination component and an oxidant generation anode serving the oxidation function. As a primary result, superior desalination capacities of approximately 87 mg g^{-1} and 36 mg g^{-1} were accomplished with NaCl concentrations of 35 g L^{-1} and 3 g L^{-1}, respectively. Moreover, this hybrid system showed a coulombic efficiency in synthetic brackish water (2.79 g L^{-1} of diverse ions) of approximately 98% and 66% for desalination and oxidation, respectively.

Second, a new HCDI system with sodium iron pyrophosphate ($Na_2FeP_2O_7$) is investigated. The overall deionization performance of $Na_2FeP_2O_7$ as the electrode capturing cations is demonstrated. The major results of the HCDI system with $Na_2FeP_2O_7$ showed a superior maximum deionization rate performance (0.08 mg g^{-1} s^{-1}) with a comparable deionization capacity (30.2 mg g^{-1}) compared to the previous HCDI system with $Na_4Mn_9O_{18}$. Furthermore, the analysis of the CDI Ragone plot was applied to investigate the hybrid behavior characteristics, high deionization capacity that originated from the high capacity of $Na_2FeP_2O_7$ and fast deionization rates resulting from the supercapacitor.

Consequently, the novel electrochemical water treatment and electrode materials can contribute to providing a new strategy to overcome the limitations of materials used for capturing anions and discovering their behavior for electrochemical water treatment.

Table of Contents

List of Figures

x

xiii

List of Tables

1. Introduction

1.1.   Research Background

Over recent decades, the lack of available water, which threatens nearly 80% of the world's population, has been considered as a critical challenge for mankind. It is expected that 3.9 billion people will suffer from limited access to water according to projections that 90% of available water will be depleted by 2025 (Service 2006, Vörösmarty, McIntyre et al. 2010, Elimelech and Phillip 2011). Electrochemical water treatment has emerged as one possible solution due to its high energy efficiency, eco-friendliness, and lack of required hazardous chemicals (Brillas, Sirés et al. 2009). It has been demonstrated in various applications such as desalination (e.g., capacitive deionization (CDI), electrodialysis (ED), and desalination batteries), heavy metal removal, wastewater treatment and water recycling (Martinez-Huitle and Ferro 2006, Oren 2008, Sadrzadeh and Mohammadi 2008, Jeong, Kim et al. 2009, Porada, Zhao et al. 2013).

Above all, electrochemical desalination has been developed by the successful convergence of materials used for energy storage with electrochemical systems for water treatment (Pasta, Wessells et al. 2012,

Zhang, Yan et al. 2012, Porada, Borchardt et al. 2013, Yin, Zhao et al. 2013, Lee, Kim et al. 2014, Suss, Porada et al. 2015, Kim, Lee et al. 2016). These techniques achieve electrochemical desalination by means of the operational principle of energy storage in supercapacitors and batteries. They provide an energy efficient desalination process, although the system performance depends heavily on electrode material.

Capacitive deionization (CDI) removes ionic species from solution by applying electric energy to carbon based electrodes and includes excellent convergence technologies combined with energy storage technology and environmental systems such as water treatment and deionization (Farmer, Fix et al. 1996, Ryoo and Seo 2003, Welgemoed and Schutte 2005, Oren 2008, Anderson, Cudero et al. 2010, Suss, Porada et al. 2015). In the CDI process, ions are stored in an electrical double layer of porous carbon electrodes, which is analogue to the principle of an electrical double-layer capacitor (Kim and Yoon 2013, Porada, Borchardt et al. 2013, Porada, Zhao et al. 2013, Kim, Lee et al. 2014). In recent decades, the technology for the synthesis of new carbon materials has advanced, the electrical double layer capacitance in porous materials has become better understood, and novel systems have been introduced. For example, advanced carbon materials have been developed in an attempt to enhance the deionization capacity in CDI, such as carbon

2

aerogel, carbon nanofiber, ordered mesoporous carbon, carbon nanotube, metal organic framework derived porous carbon, graphene derived materials and carbide derived carbon (Xu, Drewes et al. 2008, Li, Zou et al. 2010, Richard T. Mayes 2010, Li, Pan et al. 2012, Wang, Dong et al. 2012, Zhang, Wen et al. 2012, El-Deen, Barakat et al. 2013, Li, Liang et al. 2013, Porada, Borchardt et al. 2013, Wimalasiri and Zou 2013, Yin, Zhao et al. 2013, Wang, Shi et al. 2014, Yang, Kim et al. 2014, Qian, Wang et al. 2015, Xu, Pan et al. 2015). However, these carbon materials cannot fully make use of the capacitance in low electrolyte concentrations due to the overlap of the electrical double layer on its porous structure (Barbieri, Hahn et al. 2005, Li, Zou et al. 2009). Moreover, the charge efficiency, the captured ions per consumed charges, is deteriorated by the co-ion repulsion phenomenon (Avraham, Bouhadana et al. 2009, Avraham, Noked et al. 2009).

Conversely, in desalination batteries, materials that are able to capture cations or anions are required. In the case of host materials for sodium ion batteries, various potential compounds for intercalation of sodium ions have been investigated, such as $Na_{0.44}MnO_2$, λ-MnO_2, $NaFePO_4$, $Na_2FeP_2O_7$, and Prussian blue analogues (Slater, Kim et al. 2013, Kim, Hong et al. 2014, Jo, Park et al. 2015, Smith and Dmello 2016). Meanwhile, it is difficult to find suitable compounds for capturing anions. In the majority of applications, the

3

reaction of silver/silver chloride ($Ag^0 + Cl^- \rightleftharpoons AgCl$) has been used. The possibility of its use in electrochemical desalination with battery systems is limited due to the following reasons: i) the necessity of a noble metal, ii) the reaction can be used only with chloride ions, and iii) the possibility of active material dissolution (Pasta, Battistel et al. 2012, Pasta, Wessells et al. 2012, Lee, Yu et al. 2013, Trócoli, Battistel et al. 2014, Kim, Lee et al. 2015). Thus, there is an urgent requirement to develop a novel system that overcomes the current drawbacks of electrochemical desalination.

1.2.   Objectives

The aim of studies in this dissertation is to develop a novel electrochemical water treatment system and propose suitable materials for deionization and oxidation.

First of all, a novel hybrid electrochemical water treatment system consisting of an electrochemical desalination system synchronized with an oxidation process is developed. The oxidation process is a strategy for overcoming the drawbacks associated with existing electrochemical desalination systems, such as issues with anion capturing material selection, the necessity for noble metals and the possibility of active material dissolution. The hybrid electrochemical water treatment system consists of a sodium ion battery as a desalination component and an oxidant generation anode serving the oxidation function. The two components are divided by an anion exchange membrane that offers a channel for migration of anions. During the operation of this hybrid system, cations are intercalated into the cathode by applied electrical potential in the desalination component.

Second, a new HCDI system with sodium iron pyrophosphate ($Na_2FeP_2O_7$) is investigated. $Na_2FeP_2O_7$ is a promising material for sodium ion batteries due to its high capacity, low cost and environmentally benign

nature. This study attempted to investigate the overall deionization performance of $Na_2FeP_2O_7$ as the electrode capturing cations. Furthermore, the analysis of the CDI Ragone plot was applied to investigate the operational behavior of the HCDI system with $Na_2FeP_2O_7$ combined with a battery and supercapacitor compared to the conventional MCDI system.

2. Literature Review

2.1.   Electrochemical Water Treatment System

2.1.1.   Capacitive Deionization

Since the 1960s, capacitive deionization (CDI), a novel electrochemical water treatment technique, has emerged as convergence technology with energy storage material and deionization system (Farmer, Fix et al. 1996, Ryoo and Seo 2003, Welgemoed and Schutte 2005, Oren 2008, Anderson, Cudero et al. 2010, Suss, Porada et al. 2015). In CDI process, ions are stored in electrical double layer of porous carbon electrode by applying electric energy during charging step, and deionized water is produced. In discharging process, stored ions are released from electrical double layer; thereby the system is regenerated for next cycle. The principle of CDI is analogue to that of electric double-layer capacitance (EDLC) in the way that ions transport induced by electrical energy in carbon based materials (Kim and Yoon 2013, Porada, Borchardt et al. 2013, Porada, Zhao et al. 2013, Kim, Lee et al. 2014).
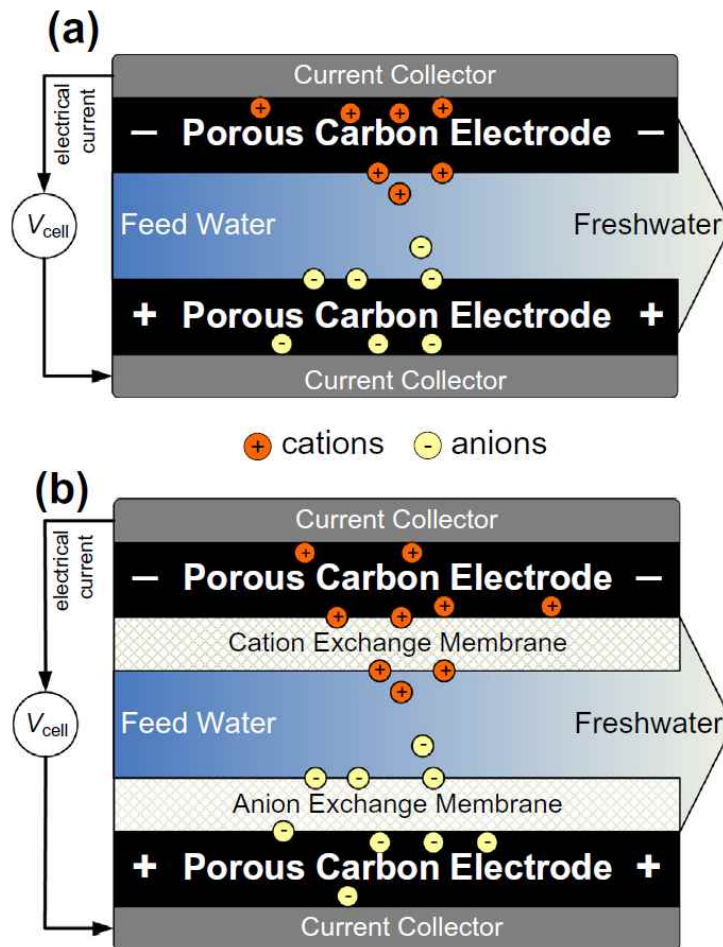
Figure 2-1. Schematic design of a cell for (Membrane) Capacitive Deionization, (M)CDI. (a) CDI; (b) MCDI, where in front of the cathode a cation-exchange membrane is placed, while an anion-exchange membrane is placed in front of the anode (Porada, Zhao et al. 2013).
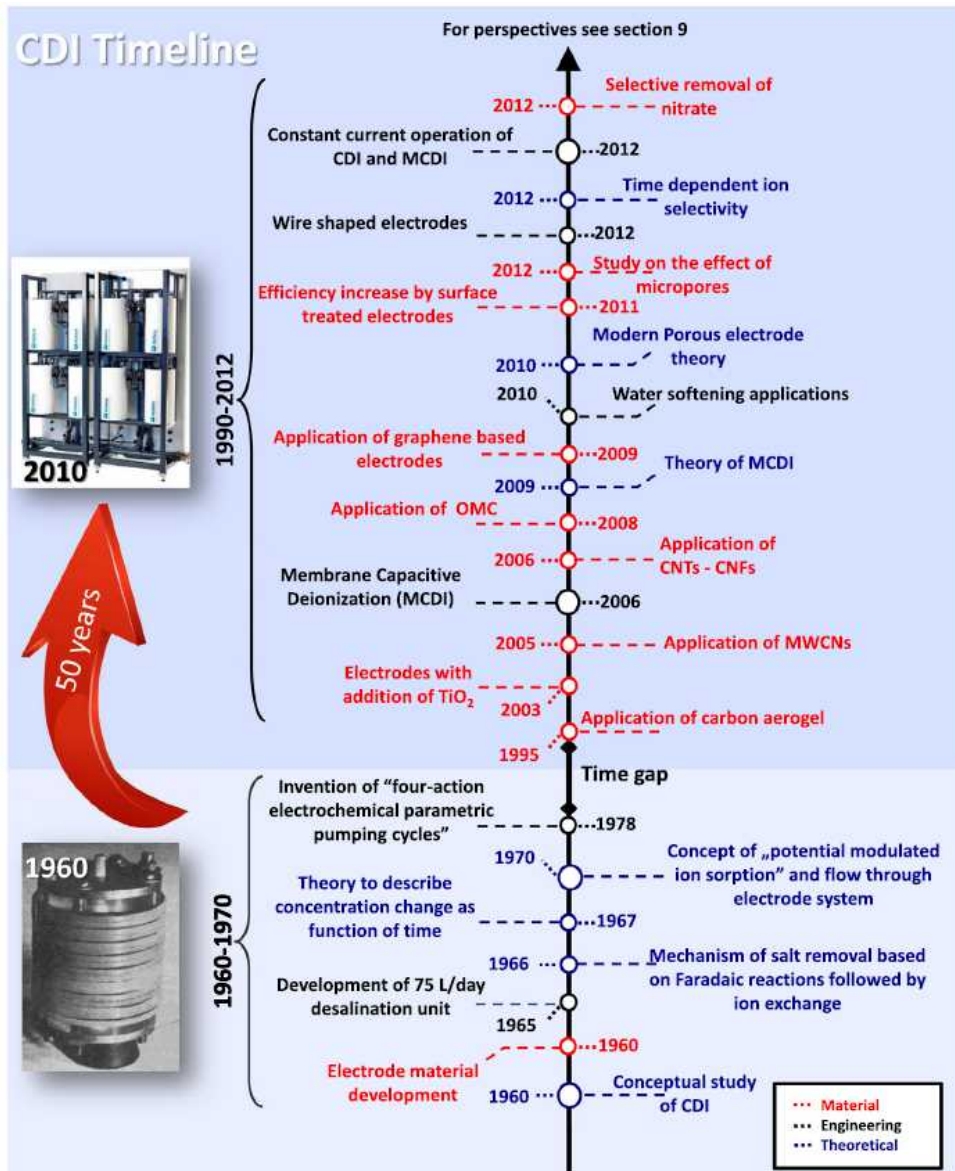
Figure 2-2. Timeline of scientific developments of CDI, indicating milestones since the inception of CDI in 1960 (Porada, Zhao et al. 2013).

9

In CDI, deionization capacity, which is a key factor of deionization performance indicating how much ions can be removed from solution, is considerably affected by capacitance of carbon materials. In recent decades, advanced carbon materials have been attempted to enhancement of deionization capacity in CDI, such as carbon aerogel, carbon nanofiber, ordered mesoporous carbon, carbon nanotube, metal organic framework derived porous carbon, graphene derived materials and carbide derived carbon, etc (Xu, Drewes et al. 2008, Li, Zou et al. 2010, Richard T. Mayes 2010, Li, Pan et al. 2012, Wang, Dong et al. 2012, Zhang, Wen et al. 2012, El-Deen, Barakat et al. 2013, Li, Liang et al. 2013, Porada, Borchardt et al. 2013, Wimalasiri and Zou 2013, Yin, Zhao et al. 2013, Wang, Shi et al. 2014, Yang, Kim et al. 2014, Qian, Wang et al. 2015, Xu, Pan et al. 2015). However, the carbon materials is not fully able to show its capacitance in low electrolyte concentration due to overlap of electrical double layer (Biesheuvel, Van Limpt et al. 2009, Zhao, Biesheuvel et al. 2009, Porada, Borchardt et al. 2013, Porada, Zhao et al. 2013). Moreover, the charge efficiency, captured ions per consumed charges, is hindered by co-ion repulsion phenomenon on carbon materials, leading to charge consumption for not only counter ion attraction but co-ion repulsion (Avraham, Bouhadana et al. 2009, Avraham, Noked et

al. 2009). Thus, it is required to overcome these drawback to achieve high

deionization capacity in CDI.

11
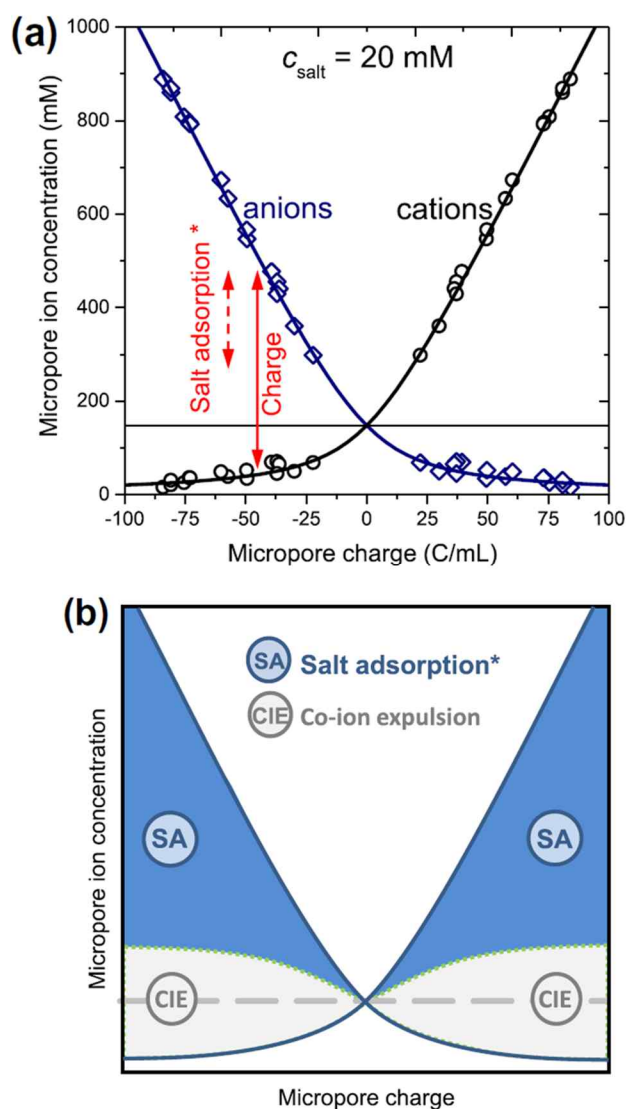
Figure 2-3. (a) and (b) Typical curves for anion and cation equilibrium adsorption in the micropores of activated carbon electrodes, expressed as moles of ions adsorbed per volume of micropores. Theoretical lines are based on the modified-Donnan model (Porada, Zhao et al. 2013).

In terms of novel system, kinetic enhancement was achieved by flow-through electrode capacitive desalination (FTE CD) (Suss, Baumann et al. 2012). In order to prevent the effect of co-ion repulsion, ion exchange membrane assisted CDI (MCDI) and ion exchange resin coated CDI were investigated (Lee, Park et al. 2006, Biesheuvel and Van der Wal 2010, Kim and Choi 2010). Continuous charging process without discharging process was successfully enabled by Flow-electrode capacitive deionization (FCDI) (Sung-il Jeon 2013, Jeon, Yeo et al. 2014, Porada, Weingarth et al. 2014). Long-term stability of carbon material was retained by altering its potential of zero charge in inverted CDI (*i*-CDI) (Gao, Omosebi et al. 2014, Gao, Omosebi et al. 2015, Gao, Omosebi et al. 2015).

Static electrode architectures

A) Flow between electrodes

B) Flow-through electrode

C) Membrane CDI

D) Inverted CDI

E) Hybrid CDI

F) Desalination battery

14

Flow electrode architectures

G) Feed in electrodes

H) Feed between electrodes

I) Membrane flow electrode
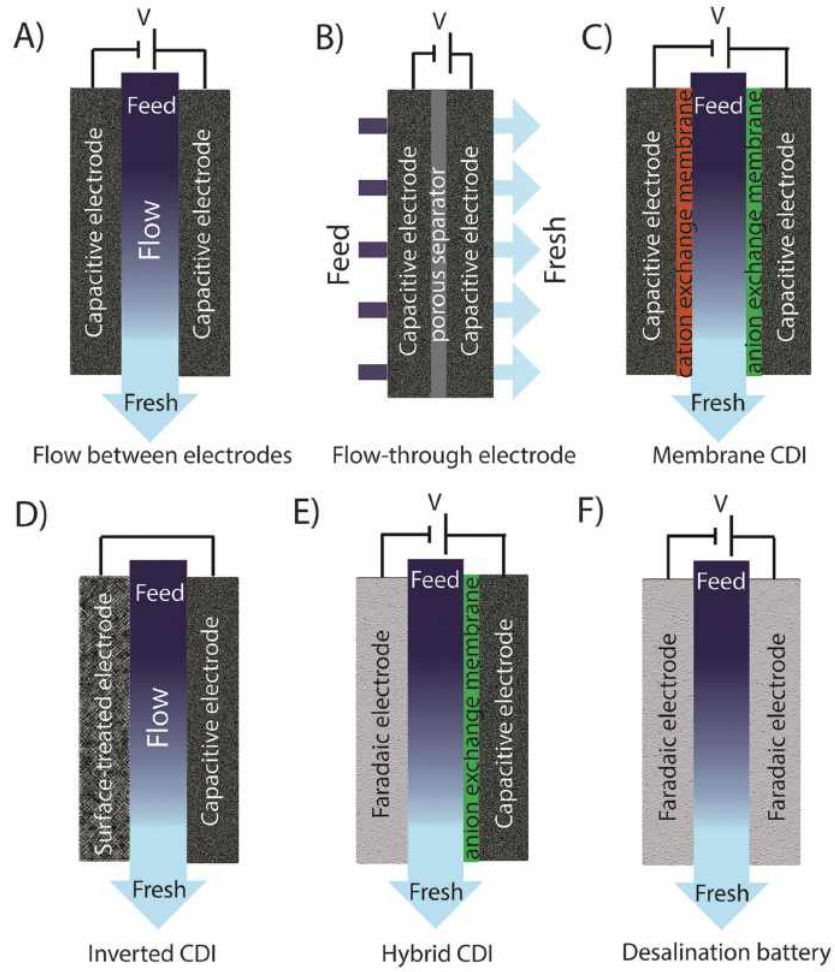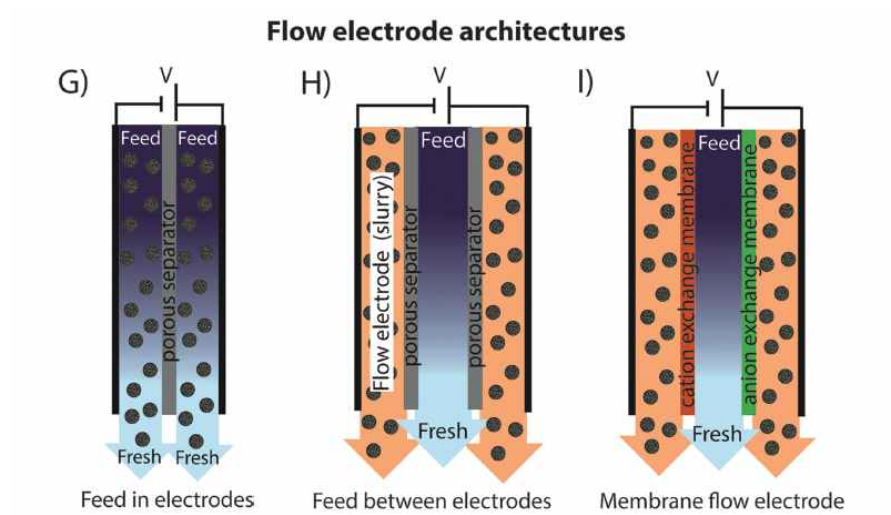
Figure 2-4. (a)–(d) CDI architectures using static electrodes, including: (a) flow between electrodes, (b) flow-through electrode, (c) membrane CDI, and (d) inverted CDI. (e) and (f) show architectures which utilize static electrodes that depart from purely capacitive behavior, including (e) hybrid CDI, and (f) a desalination battery. (g)–(i) show CDI architectures with flow electrodes, including systems with (g) feed-in electrodes, (h) feed-between electrodes, and (i) membrane flow electrode CDI (Suss, Porada et al. 2015).

2.1.2.　　**Desalination Battery**

In order to enhance the deionization capacity, a new concept of a desalination battery was proposed (La Mantia, Pasta et al. 2011, Pasta, Wessells et al. 2012). The system consists of a sodium manganese oxide and silver/silver chloride electrodes. The $Na_{2-x}Mn_5O_{10}$ (NMO) nanorods and silver electrode were utilized to capture sodium ions and chloride ions as following chemical reaction

$$5MnO_2 + 2Ag + 2NaCl \leftrightarrow Na_2Mn_5O_{10} + 2AgCl$$
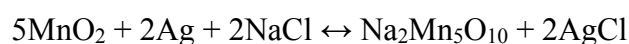
Due to the high specific charge storage capacity ($\sim$ 35 mAh g^{-1}), low cost and benign environmental impact, NMO is one of ideal materials for capturing cations. Moreover, the NMO prepared by a polymer synthesis method exhibits fast ion transfer on the interface between the electrode and electrolyte because of its nanorods shape.

　　　The desalination battery showed energy efficient operation in sea water desalination, which the energy of 0.29 Wh l^{-1} was required for 25% removal of NaCl, indicating this system can compete with reverse osmosis (0.2 Wh l^{-1}) under sea water desalination. Since this system generates the

energy in discharging process and consumes it in charging process, energy efficient operation can be accomplished. In respect to coulombic efficiency during operation, approximately the coulombic efficiency of 80% was reported due to reduction of oxygen and formation of OH^-. In addition, it was reported that the intercalation of Ca^{2+}, Mg^{2+} in NMO structure due to these crystal ionic radii of cations.

Although this desalination battery showed promising energy efficient deionization process even in the salinity level of sea water, the limitation of silver electrode, such as low conductivity of silver chloride, cost, formation of silver sulfate at high potential (0.65 V vs. NHE) and materials dissolution should be overcome.

17
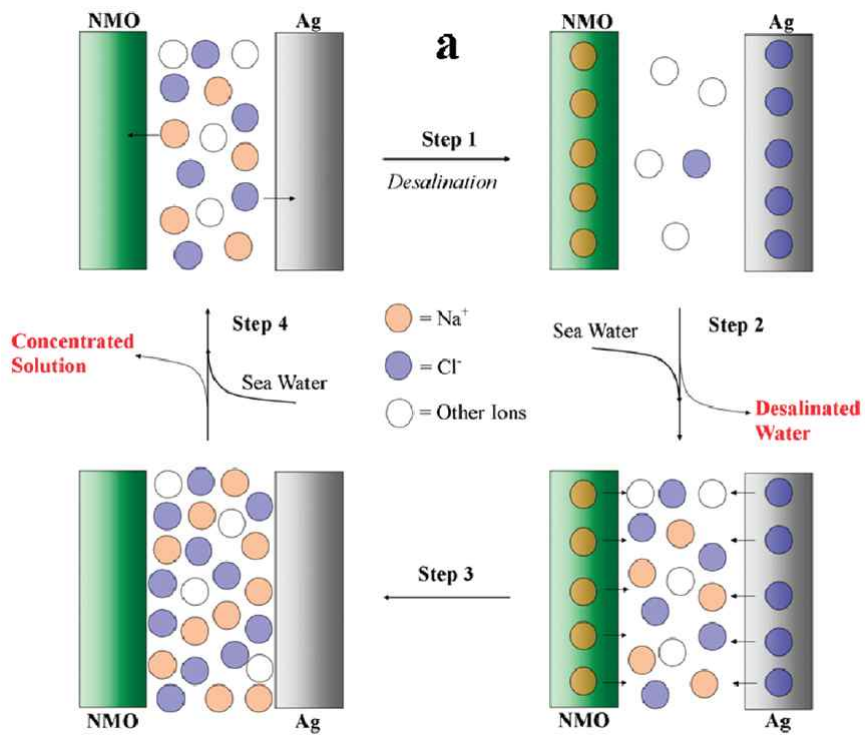
Figure 2-5. Schematic representation of the working principle behind a complete cycle of the desalination battery, showing how energy extraction can be accomplished: step 1, desalination; step 2, removal of the desalinated water and inlet of sew water; step 3, discharge of Na^+ and Cl^- in seawater; step 4, exchange to new seawater (Pasta, Wessells et al. 2012).

Table 2-1. ICP-OES/ICP-MS: Coulombic Efficiencies and Selectivity for

Anions and Cations (Pasta, Wessells et al. 2012).

ion	Na^+	K^+	Mg^{2+}	Ca^{2+}	Cl^-	SO_4^{2-}
sea water (mg/L)	11250	450	1400	450	18500	2750
25% removal (mg/L)	9840	430	1130	280	14470	2750
$\eta_{C,25}$	47%	<1%	9%	3%	87%	control
50% removal (mg/L)	7860	390	860	180	11430	2750
$\eta_{C,50}$	57%	<1%	9%	3%	76%	control

2.1.3. Hybrid Capacitive Deionization

Recently Hybrid CDI (HCDI) was proposed as a novel concept of CDI, which is a combined CDI system of material for sodium ion batteries (SIBs) and activated carbon (Lee, Kim et al. 2014). The HCDI with sodium manganese oxide ($Na_4Mn_9O_{18}$) was enabled by combining materials for SIBs and supercapacitor. The HCDI system utilizes the intercalation of Na^+ in the $Na_4Mn_9O_{18}$ and adsorption of Cl^- on the surface of the activated carbon electrode. As utilizing carbon electrode to capture chloride ions, this system copes with the difficulties of silver electrode. Furthermore, since $Na_4Mn_9O_{18}$ exhibits higher capacity ($40 \sim 50$ mAh g^{-1}), corresponded to the capacitance of more than 300 F g^{-1}, than that of activated carbon (~ 120 F g^{-1}), HCDI system is able to show superior deionization capacity (mg of removed NaCl per g of electrodes) than typical CDI system, which symmetric two carbon electrodes are employed.

As a major result, the HCDI system showed the deionization capacity of 31.2 mg g^{-1} that is the highest record ever reported. Compared to typical CDI and MCDI system, the HCDI system exhibited 230% and 140% of deionization capacity, respectively. Moreover, stability of the $Na_4Mn_9O_{18}$/activated carbon system was demonstrated. Approximately 100%

20

of coulombic efficiency was retained during 300 cycles in the galvanostatic cycling test.

However, even though HCDI showed great promise as novel CDI system, the advance of HCDI has been limited due to the synthesizing new material for SIBs and its convergence with desalination application. For the further understanding of HCDI, it has been required that investigation of material for SIBs as an electrode for deionization.
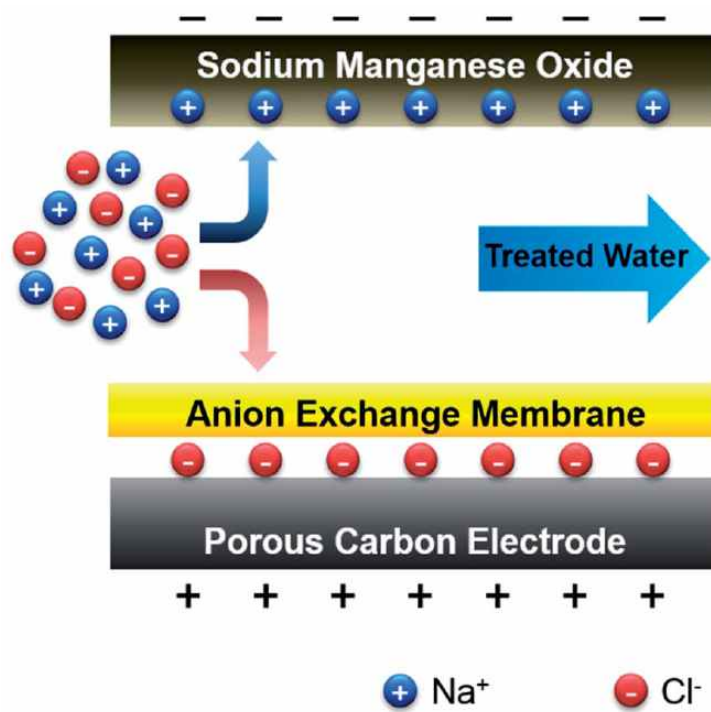
Figure 2-6. Schematic diagram of desalination via HCDI. The HCDI system consists of an NMO electrode, anion exchange membrane, and porous carbon electrode (Lee, Kim et al. 2014).
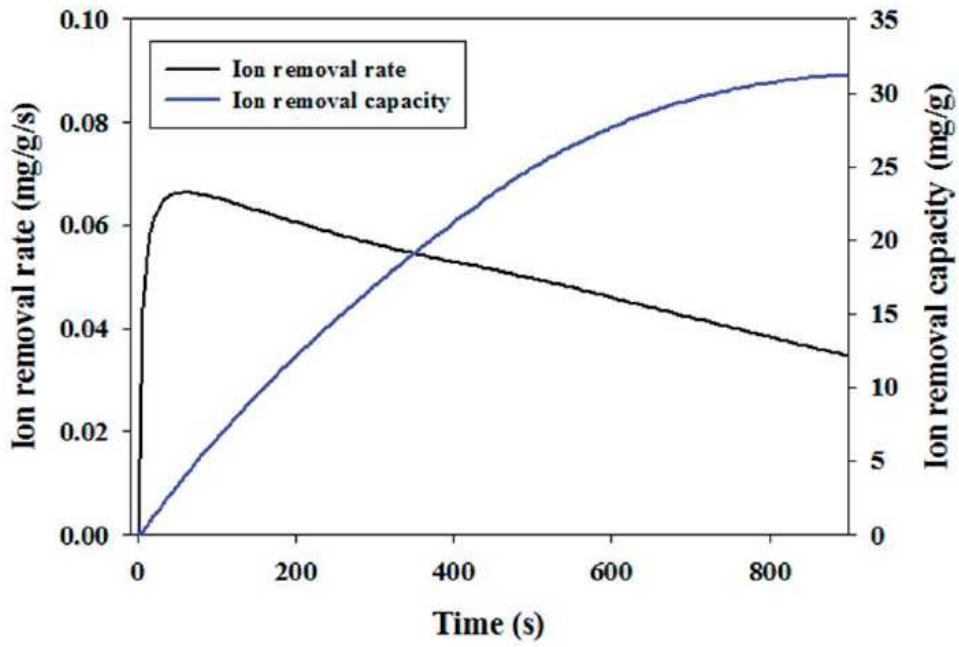
Figure 2-7. Ion removal capacity and accumulated ion removal rate of HCDI during the third ion capturing step, represented as the mass of deionized ionic charge (mg) per total mass of the NMO and activated carbon electrodes (g) (Lee, Kim et al. 2014).

2.2. Materials of Electrochemical Water Treatment for Deionization and Oxidation

2.2.1. Materials for Deionization

Among a variety of investigated materials for sodium ion batteries (SIBs), certain materials that are able to stably work at the potential range preventing the oxygen and hydrogen evolution can be applied to applications in the aqueous system. For decades, materials for aqueous sodium ion batteries (SIBs) have intensively investigated, such as $Na_{0.44}MnO_2$, λ-MnO_2, $NaFePO_4$, $Na_2FeP_2O_7$, and Prussian blue analogues due to its practicability for large-scale applications (Kim, Hong et al. 2014).

$Na_{0.44}MnO_2$ is the most extensively utilized as the electrode material for intercalation/deintercalation of sodium ions. Since the redox potentials of intercalation/deintercalation of sodium ions in $Na_{0.44}MnO_2$ are located at the 0.29, 0.51, and 0.74 V vs. NHE, working potential is suitable in aqueous system. Moreover, the orthorhombic crystal structure of $Na_{0.44}MnO_2$ facilitates rapid diffusion of sodium ions through three dimensionally interconnected S-shape tunnels. In respect to the charge storage capacity,

24

approximately 45 mAh g^{-1} and 20 mAh g^{-1} were obtained at a C/8 and 18 C rate, respectively.

Recently $Na_2FeP_2O_7$ was investigated as a novel material with high specific capacity (~90 mAh g^{-1} at a 1C rate) and fast kinetic characteristic in aqueous electrolyte. The triclinic structure under P1 space group of $Na_2FeP_2O_7$ that consists of infinite metal polyhedral and pyrophosphate group enables the migration of sodium ions. The redox potentials of $Na_2FeP_2O_7$ are located at -0.23 V, 0.18 V, 0.29 V and 0.41 V vs. NHE, of which the working potential of $Na_2FeP_2O_7$ is negatively situated compared to that of $Na_{0.44}MnO_2$.
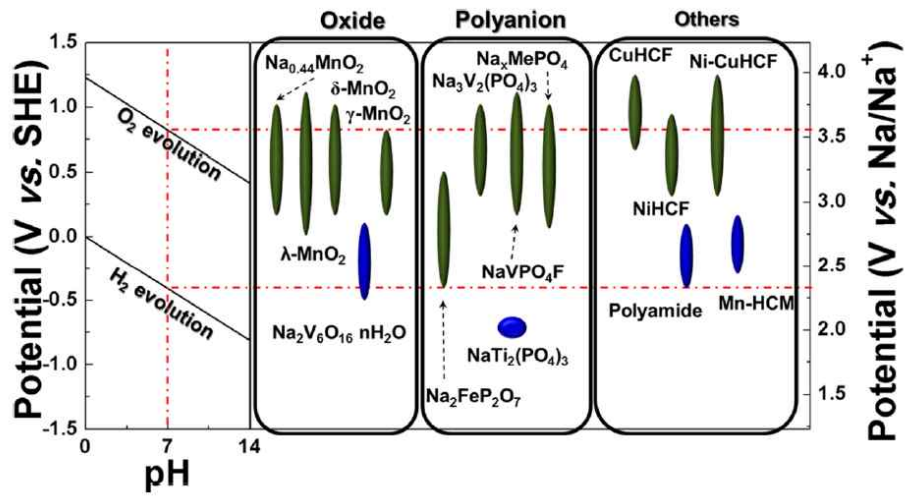
Figure 2-8. Electrode materials for ARSBs. The potentials of the electrode materials are described vs SHE and Na^+/Na. The red dotted line illustrates H_2 and O_2 evolution limits in a neutral aqueous solution (Kim, Hong et al. 2014).
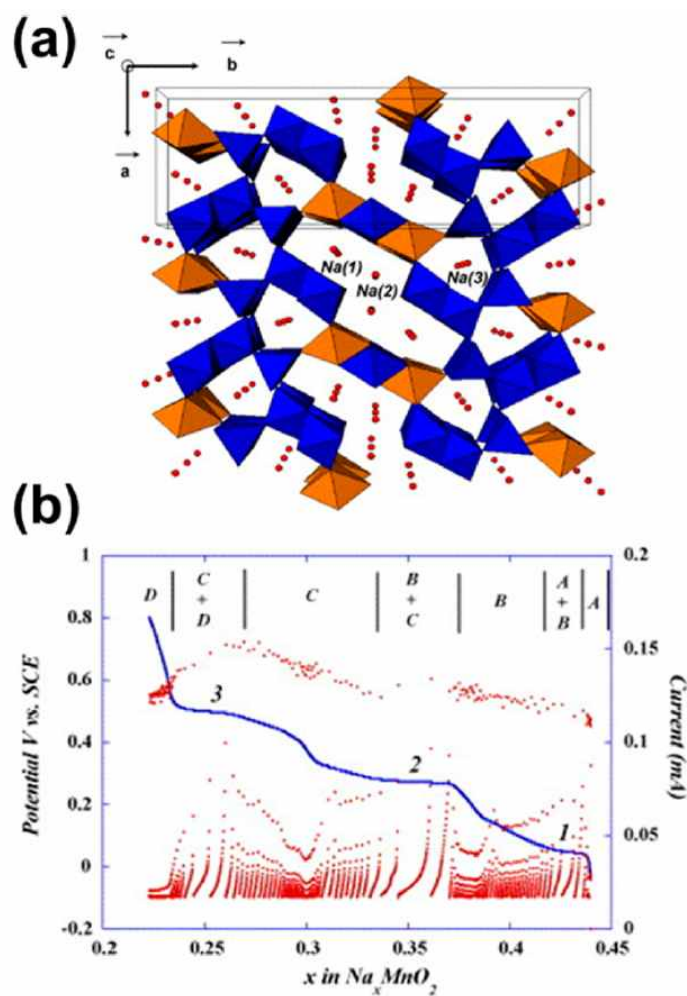
Figure 2-9. (a) Structural schematics of $Na_{0.44}MnO_2$. The Na^+ ions are indicated by red spheres. (b) PITT profiles obtained at a C/200 rate using SCE as a counter electrode with a step of 0.005 mV in 1 M NaNO3 electrolyte (Sauvage, Baudrin et al. 2007, Sauvage, Laffont et al. 2007).
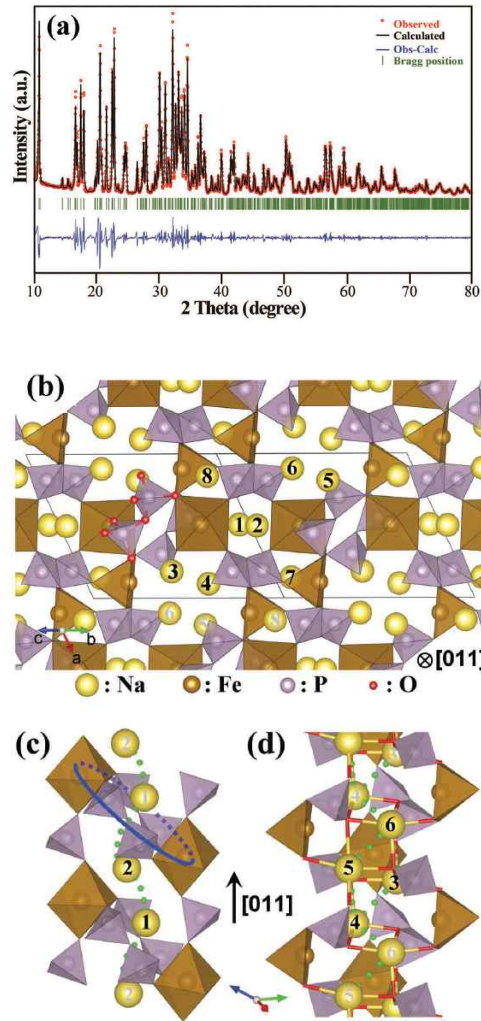
Figure 2-10. (a) The XRD spectrum and whole pattern fitting of $Na_2FeP_2O_7$ (b) The crystal structure of $Na_2FeP_2O_7$ projected along the [011] direction showing the different sodium sites and the arrangement of octahedral and polyhedral units. The sodium migration channels for (c) the Na1 and Na2 sites and d) the Na3–Na6 sites (Kim, Shakoor et al. 2013).

2.2.2. Materials for Oxidation

Electrochemical advanced oxidation process (EAOP) has gained interest for water treatment. In EAOP, an electrode functions as electro-catalyst that assists efficient generation of various oxidants such as reactive chlorine species (e.g., Cl_2, HOCl and Cl•), reactive oxygen species (e.g., H_2O_2, OH• and O_3). The selection of electrode material significantly affects the efficiency.

Electrodes based on mixed metal oxide (e.g., IrO_2, RuO_2, PbO_2, SnO_2), which is well-known for commercial trade name Dimensionally Stable Anode (DSA®), have been extensively used for chlor-alkali process. These mixed metal oxide electrodes were classified to active anodes that have a low overpotential for oxygen evolution, providing efficient chlorine evolution. Thus, pollutants and organics are oxidized in the presence of chloride. Boron-doped diamond (BDD) electrodes have been investigated due to the high overpotential for oxygen evolution, providing formation of OH• on the electrode surface. Thus, BDD electrodes were classified to non-active anodes and utilize direct oxidation process of pollutants and organics by electrolysis.

However, need of precious metal precursors and relatively little investigations for electrode and reaction in the part of electrochemical reduction can be major obstacles to utilize EAOP in the practical applications (e.g., point-of-use drinking water system and potable water treatment).

Recently as a novel material for anode, a Blue TiO2 nanotube was reported, which demonstrated the generation of oxidants through TiO_2 nanotube treated by cathodic polarization (Kim, Kim et al. 2014). The TiO_2 nanotube can be easily fabricated by anodization in the electrolyte containing H_2O/NH_4F with ethylene glycol under the constant voltage operation. After cathodic polarization treatment, the novel features in the TiO_2 nanotube emerged, which exhibited blue coloration and remarkably enhanced electrocatalytic activity in oxygen evolution reaction, resulting from irreversible proton intercalation. The Blue TiO_2 nanotube showed a potential as a novel anode for generating chlorine and OH• without containing precious metal compounds. The amount of chlorine generation on the Blue TiO_2 nanotube was comparable with that on the DSA®. In addition, the efficiency of OH• generation on the Blue TiO_2 was also comparable with that on the BDD. It implies that the Blue TiO_2 possesses inter-mediate electrochemical characteristic between active anode and non-active anode.
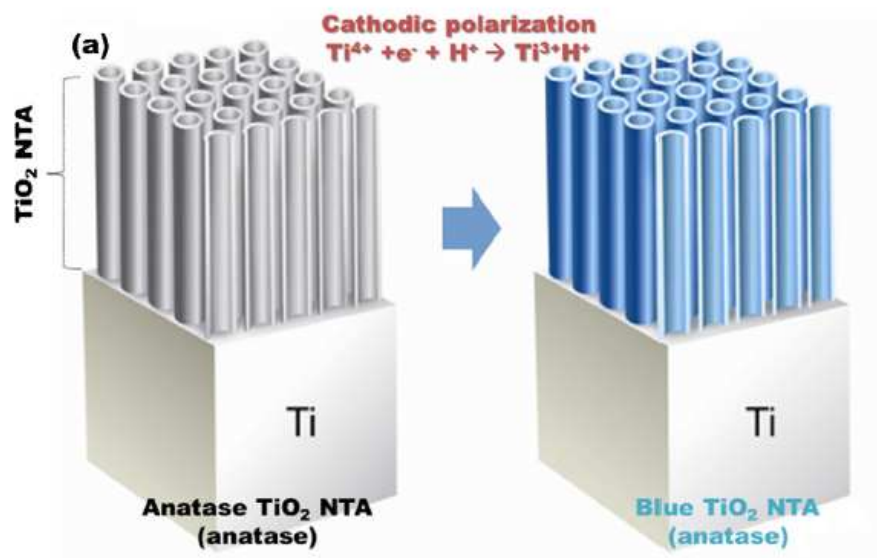
Figure 2-11. Scheme for fabricating the Blue TiO$_2$ NTA from the anatase

TiO$_2$ NTA with the simple cathodic polarization (Kim, Kim et al. 2014).
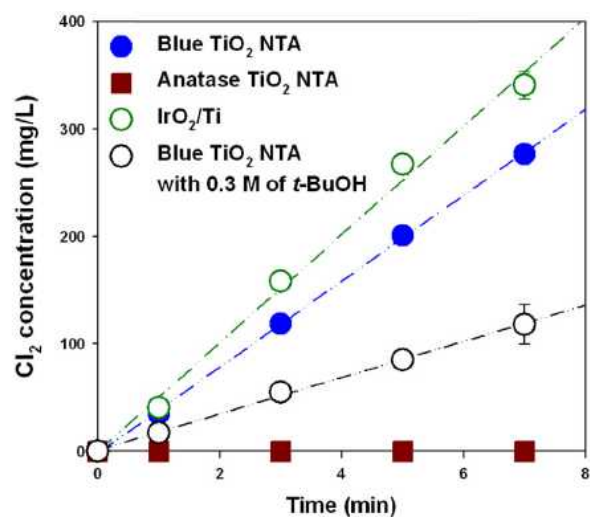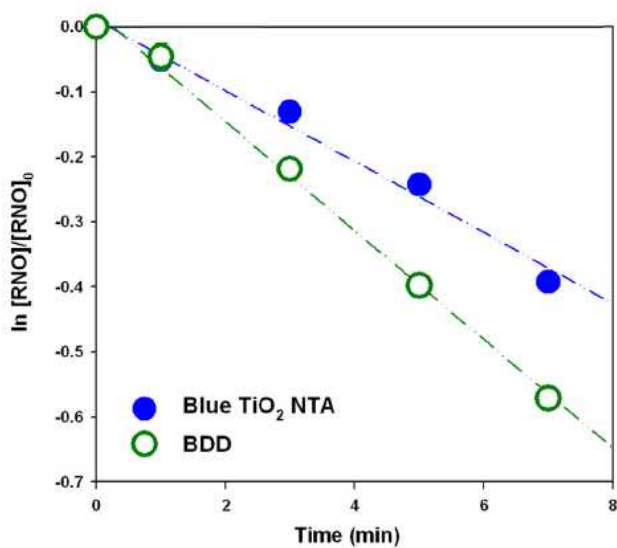
Figure 2-12. (a) Evolution of chorine (Cl_2) on the Blue TiO_2 NTA, the anatase TiO_2 NTA and the commercial IrO2/Ti and effect of hydroxyl radical (•OH) scavenger in evolution of Cl_2 on Blue TiO_2 NTA (b) between the Blue TiO_2 NTA and the commercial BDD electrode (Kim, Kim et al. 2014).

3. Hybrid Electrochemical Water Treatment System for Deionization and Oxidation

3.1. Introduction

In this study, a novel hybrid electrochemical system consisting of an electrochemical desalination system synchronized with an oxidation process is proposed (Figure 3-1). This hybrid system is realized by combining a cathode for capturing cations with an oxidant generation anode. As described in Figure 3-1, this hybrid system consists of a desalination component and an oxidation component. The two are divided by an anion exchange membrane that offers a channel for migration of anions.
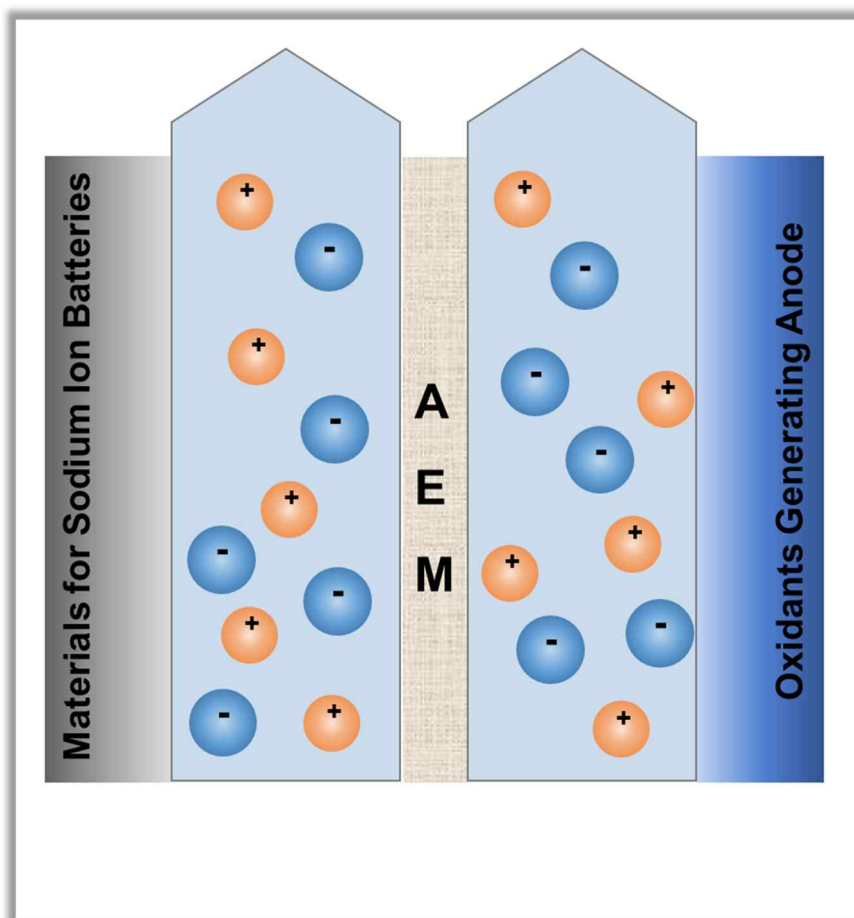
Figure 3-1. Schematic of a novel hybrid electrochemical water treatment system consisting of an electrochemical deionization system synchronized with the oxidation process.

During operation of this hybrid system, cations are intercalated into the cathode by an applied electrical potential. Simultaneously, anions diffuse into the oxidation component through the anion exchange membrane in order to retain a neutral charge in the desalination component. At the same time, oxidation reactions occur on the anode of the oxidation component, maintaining the charge balance in the oxidation component and facilitating the diffusion of anions from the desalination component. In water containing a high concentration of chloride ions, chlorine can be generated and utilized in the disinfection or oxidation application of water treatment. A sodium manganese oxide, which is a representative material in sodium ion batteries, was selected as a cathode for capturing cations. A Blue TiO_2 nanotube, recently reported as a novel anode, was adopted as an oxidant generating anode due to its high efficiency for chlorine generation without the use of precious metals (Kim, Kim et al. 2014).

35

Desalination & Oxidation

(a)

Materials for Sodium Ion Batteries

Deionized Water

Intercalation

Oxidants Generation

A E M

Oxidation

Oxidants Generating Anode

36
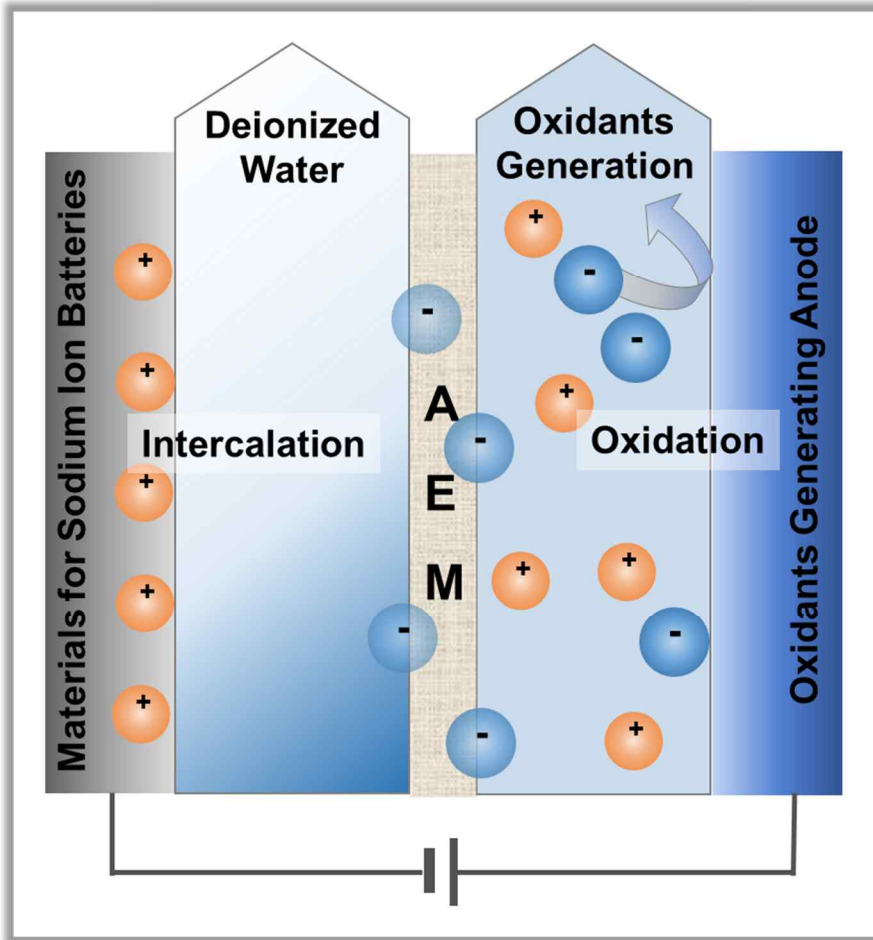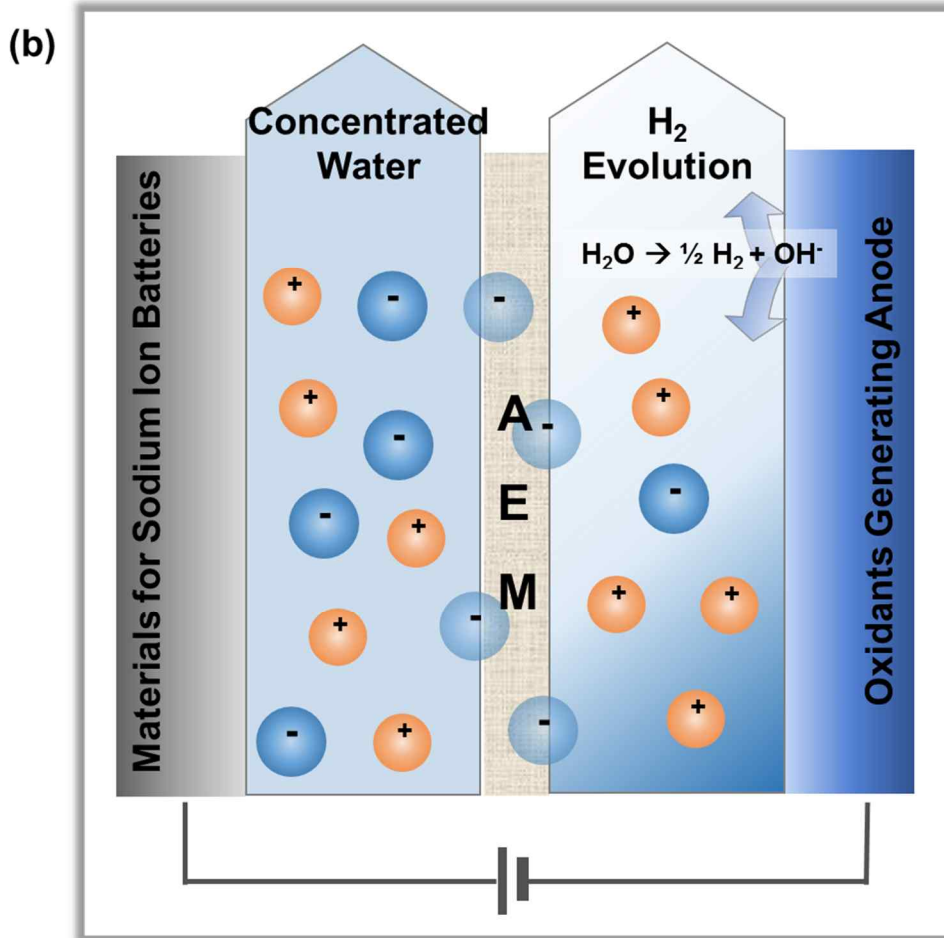
Figure 3-2. Schematic of operating the hybrid electrochemical water treatment system (a) desalination and oxidation and (b) concentration and hydrogen evolution.

3.2. Experimental

3.2.1. Preparation of sodium manganese oxide ($Na_{0.44}MnO_2$)

The $Na_{0.44}MnO_2$ was synthesized via solid state reaction with Na_2CO_3 and Mn_2O_3 (Sigma-Aldrich, USA), following the procedure (Lee, Kim et al. 2014). These chemicals were mildly mixed at a molar ratio of 0.484 : 1 (Na_2CO_3 : Mn_2O_3). Then, the mixed powder was pelletized and annealed at 500°C for 5 h under air condition and cooled to room temperature. The product was re-pelletized and annealed at 900°C for 12 h under atmosphere condition. $Na_{0.44}MnO_2$ electrode was fabricated by a slurry mixture of prepared powder (80 wt%), carbon black (Super-P^{TM}, TIMCAL Graphite and Carbon Inc., Switzerland, 10 wt%) and polytetrafluoroethylene (PTFE, Sigma-Aldrich, USA, 10 wt%). The mixture was treated by roll press machine to prepare sheet-type electrode with approximately 300 μm of thickness. The electrode was dried in a vacuum oven at 60°C for 12 h to remove remaining solvent.

3.2.2. Preparation of blue TiO₂ nanotube on meshed Ti substrate (m-Blue TiO₂ NTs)

The m-Blue TiO$_2$ NTs was fabricated by following the procedures of anodization and cathodic polarization reported in literatures (Kim, Kim et al. 2014). First, titanium mesh degreased by ultrasonication in acetone and platinum were used as the anode and cathode, respectively. Anodization was conducted in the electrolyte of H$_2$O (2.5 wt%)/NH$_4$F (0.2 wt%) with ethylene glycol for 5 h under constant voltage (40 V) at room temperature. The anodized TiO$_2$ nanotube on meshed Ti substrate was annealed at 450°C for 1 h under air condition. Then, the electrode was treated by cathodic polarization under constant current (17 mA cm^{-2}) for 90 s in phosphate buffer electrolyte ([KH$_2$PO$_4$]$_0$ = 0.1 M with NaOH, pH ~7.2), leading to the m-Blue TiO$_2$ NTs.

3.2.3. Characterization of prepared electrodes

The prepared electrodes were characterized by field emission scanning electron microscopy (FE-SEM, JSM 6700F, JEOL Ltd, Japan), and the crystalline structure was analyzed by X-ray powder diffraction (HR-XRD, Bruker D8 Discover X-ray Diffractometer, Germany). Electrochemical characterization of the prepared electrodes was measured by cyclic voltammetry (CV) and staircase linear sweep voltammetry (SLSV) with a potentiostat (PARSTAT 2273, Princeton Applied Research, USA). Galvanostatic charge/discharge was conducted with a battery cycler (WBCS 3000, WonA Tech Co., Korea).

3.2.4. Operations of the hybrid system for deionization and oxidant generation

The hybrid water treatment system consists of a deionization component and an oxidation component, which are separated by an anion exchange membrane (AMV, AGC engineering Co., Japan). Operation of the hybrid system was carried out with $Na_{0.44}MnO_2$ and m-Blue TiO_2 NTs. The electrolyte volumes of the deionization cell and the oxidant generation cell were 41 mL and 90 mL, respectively. Prior to installation of the system, the $Na_{0.44}MnO_2$ electrode was treated by a pre-charging process in which a potential of 0.9 V (vs. Ag/AgCl) was applied for 30 min, providing defect sites to Na in $Na_{0.44}MnO_2$ (Lee, Kim et al. 2014). The performance of the hybrid system was tested in synthetic brackish water (total amount of salt: ~ 2.79 g L^{-1}), which included sodium, calcium, magnesium, chloride and sulfate ions (the details are presented in Table 1). The current density was 50 mA g^{-1} based on $Na_{0.44}MnO_2$ (~ 1 C: theoretical capacity of 50 mAh g^{-1}) and 3.5 mA cm^{-2} based on m-Blue TiO_2 NTs (Lee, Kim et al. 2014). Additionally, the system was tested in the NaCl concentration range of 3 g L^{-1} to 35 g L^{-1} based on the salinity levels of brackish water and sea water.

The amount of deionized ions was estimated from the change in concentration of cations and anions in the deionization cell measured through ion chromatography (IC, DX-120, DIONEX Co., Ltd., USA). The desalination capacity was expressed by the total mass of deionized ions per mass of the employed electrode. The amount of accumulated reactive chlorine in the oxidation cell was measured by the N,N-diethyl-p-phenylenediamine (DPD) colorimetric method using a spectrophotometer (DR/2010, HACH Co., USA) at a wavelength of 530 nm (Jeong, Kim et al. 2009). The coulombic efficiency for chlorine generation was estimated by the following Equation (1):

$$\eta_{Cl_2} = \frac{n \times V \times F \times [Cl_2]_{DPD}}{I \times t} \quad (1)$$

where n is the number of consumed charges, V is the volume of electrolyte (L), F is the Faraday constant (96485 C equi^{-1}), $[Cl_2]_{DPD}$ is the concentration of chlorine (mol L^{-1}), I is the applied current (A) and t is the operation time.

3.3.   Results and Discussion

Table 3-1 presents the overall performance of hybrid electrochemical water treatment system for desalination and oxidation as the hybrid system operated in the synthetic brackish water (sodium: 873.6 mg L^{-1}, calcium: 63.2 mg L^{-1}, magnesium: 85.5 mg L^{-1}, chloride: 1547.1 mg L^{-1}, sulfate: 219.8 mg L^{-1}). Deionization occurred in the $Na_{0.44}MnO_2$, and simultaneously, oxidation occurred in the m-Blue TiO_2 NTs. As shown in Table 1, this hybrid system demonstrated effective deionization capability with coulombic efficiency of approximately 98% considering the cations (sodium, calcium, and magnesium ions). Approximately 68% of the charges were consumed for capturing sodium ions, which composed the majority of the synthetic brackish water. Notably, despite $Na_{0.44}MnO_2$ being a representative host material for sodium intercalation, approximately 30% of charges were consumed for capturing magnesium ions and calcium ions. The high removal ratio of the divalent ions magnesium and calcium is possibly explained by their smaller or equivalent atomic size and high electrostatic force of divalent ions compared to those of sodium ions (Pasta, Wessells et al. 2012).

However, no notable difference was observed in the removal ratio of the anions (chloride and sulfate). It is plausible to explain that the anions do not selectively diffuse through the anion exchange membrane due to their similar ionic mobility in water (Cl^-: 7.91 10^{-8} m^2 s^{-1} V^{-1}, SO_4^{-2} : 8.29 x 10^{-8} m^2 s^{-1} V^{-1}) (Bard and Faulkner 2001). Furthermore, as shown in Table 1, this hybrid system demonstrated a coulombic efficiency of approximately 66% for chlorine generation in the synthetic brackish water, and the rest of the charges were presumed to be utilized for oxygen evolution. This result indicates that the m-Blue TiO_2 NTs efficiently functions as the anode for chlorine generation in the low concentrations of synthetic brackish water (~ 1,547 mg L^{-1} of Cl^-) and is supported by the SLSV in Figure 3-3 (Kuhn and Mortimer 1972, Rajkumar, Kim et al. 2004).

Table 3-1. The overall performance of hybrid electrochemical water treatment system for desalination and oxidation in the synthetic brackish water (The current density: 1 C, 50 mA g^{-1} based on Na$_{0.44}$MnO$_2$, 3.5 mA cm^{-2} based on Blue TiO$_2$ NTs)

	Desalination Cell					Oxidation Cell
	Na$^+$	Ca^{2+}	Mg^{2+}	Cl$^-$	SO$_4^{2-}$	Cl$_2$ generation
C$_i$ / mg L^{-1}	873.6	63.2	85.5	1547.1	219.8	0
C$_f$ / mg L^{-1}	615.9 ± 1.4	28.7 ± 1.1	46.5 ± 1.0	1032.6 ± 7.9	136.9 ± 1.0	173.3
ΔC / %	29.5	54.4	45.9	33.2	37.8	—
Coulombic Efficiency / %	68	10	20	88	10	66
	98 (Total)					

Figure 3-3 shows the anodic SLSV of the Blue TiO_2 NTs in 1 M of NaCl and Na_2SO_4. As shown in Figure 3-3, remarkably, a difference of anodic onset potentials was observed in the Blue TiO_2 NTs depending upon the species of anion (Cl, SO_4^{2-}). In the presence of chloride ions (1 M of NaCl), the onset was measured near 1.6 V (vs. Ag/AgCl KCl sat'd), whereas it was over 2 V (vs. Ag/AgCl KCl sat'd) in the absence of chloride ions (1 M of Na_2SO_4). The m-Blue TiO_2 NTs exhibited lower onset potential in the presence of chloride ions, which provides insight into the favorable characteristic for chlorine evolution compared to that of oxygen evolution. Although the theoretical potential of oxygen evolution at a neutral pH (0.62 V vs. Ag/AgCl) is much lower than that of chlorine evolution (1.16 V vs. Ag/AgCl), the chlorine evolution was noted to be kinetically favorable due to abstraction of four electrons for the oxidation of H_2O to O_2 (Hoganson and Babcock 1997). This efficient property of the m-Blue TiO_2 NTs for chlorine generation led to the stability of this hybrid system without accumulation of diffused anion from desalination cell.

46
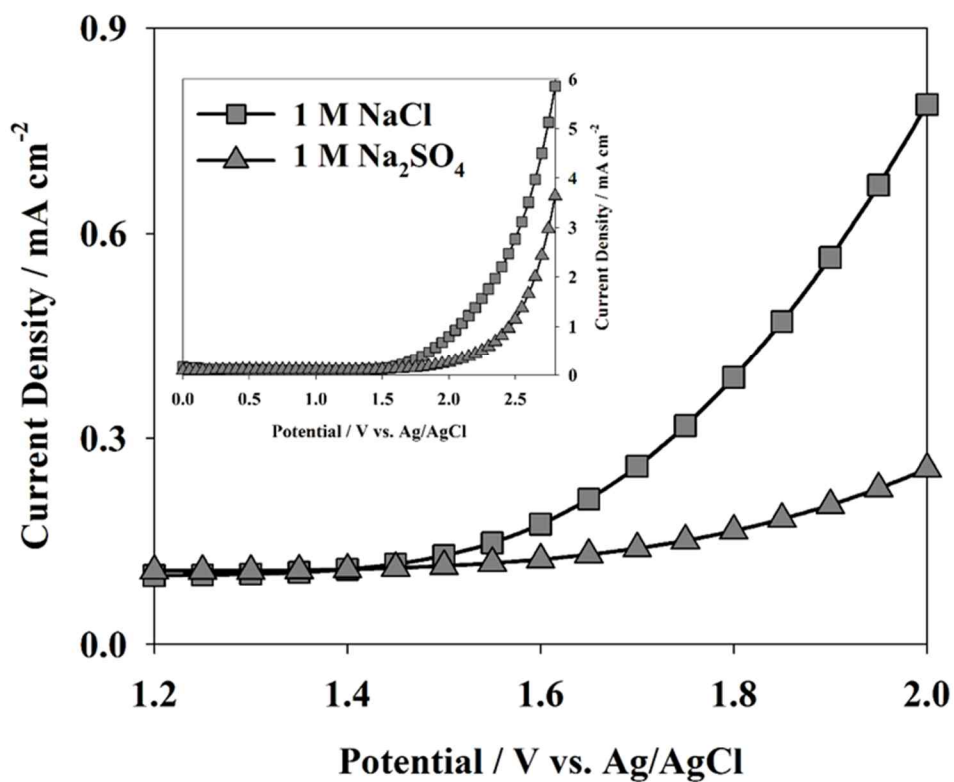
Figure 3-3. SLSV of the Blue TiO2 NTs in 1 M of NaCl and Na_2SO_4. SLSV was conducted with a 50 mV step height and 1 min step width, and the scan rate was 0.83 mV s^{-1}. Inset showed wide range (0 – 2.5 V vs. Ag/AgCl) of the SLSV.

Figure 3-4 shows the voltage profile of the hybrid system that consisted of each potential profile of the m-Blue TiO_2 NTs and the $Na_{0.44}MnO_2$ measured in the corresponding condition in Table 3-1. As shown in Figure 3-4, the hybrid system was operated under a range of cell voltages from 2.2 V to 3.0 V. At the initial operation, the cell voltage was measured to be 2.2 V, while it increased to 3.0 V at the end of operation. This resulted from the increasing over-potential for chlorine generation of the m-Blue TiO_2 NTs (2.8 V to 3.2 V vs. Ag/AgCl) and the decreasing potential of the $Na_{0.44}MnO_2$ (0.6 V to 0.2 V vs. Ag/AgCl) by the intercalation reaction of cations. Overall, estimating the required energy based on the result in Table 3-1 and Figure 3-4, this hybrid system is able to deionize 33% ions in 1 L of synthetic brackish water and produce 4.3 g of chlorine using approximately 1.3 Wh of energy.
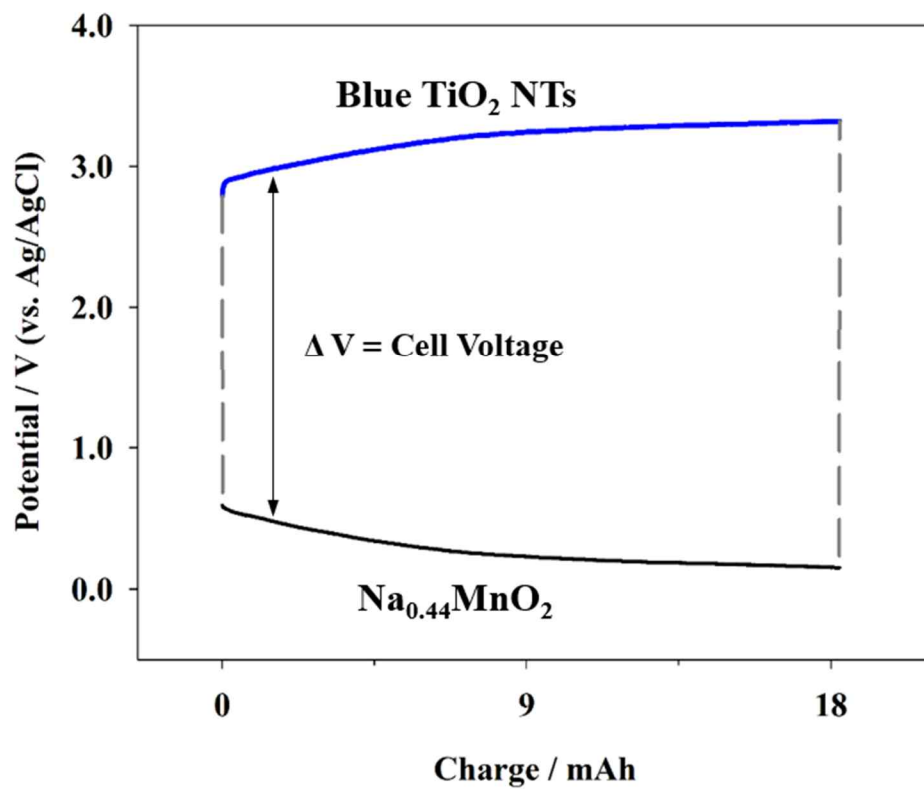
Figure 3-4. Voltage profile of hybrid electrochemical water treatment system that consisted of each potential profile of the m-Blue TiO$_2$ NTs and the Na$_{0.44}$MnO$_2$ measured in the corresponding condition in Table 3-1.

Figure 3-5 (a) and (b) show the specific capacity of the $Na_{0.44}MnO_2$ via the discharging curves and its desalination capacity (the amount of deionized ions per the mass of employed electrode) in the concentration range of 3 g L^{-1} to 35 g L^{-1} of NaCl (representing the salinity level from brackish water to sea water), respectively. As shown in Figure 3-5 (a), the $Na_{0.44}MnO_2$ exhibited its high specific capacity with increasing concentration of NaCl, which allows more ions to be accessible to the interfaces of electrode. For instance, the specific capacity in 3 g L^{-1} of NaCl was approximately 18 mAh g^{-1}, whereas it increased to approximately 40 mAh g^{-1} in 35 g L^{-1} (more than twice the specific capacity). This implies that twice as many sodium ions can be intercalated into the $Na_{0.44}MnO_2$.

In Figure 3-5 (b), the deionization capacity of sodium ions (gray) and total desalination capacity of NaCl (gray + white) are presented depending on the concentration of NaCl. Notably, world record-level desalination capacity of approximately 87 mg g^{-1} was achieved in 35 g L^{-1} of NaCl. The desalination capacity was approximately 36 mg g^{-1} in 3 g L^{-1} of NaCl. Note that these desalination capacities of this hybrid system were much higher than that in CDI (~ 14 mg g^{-1} in 0.6 g L^{-1}) and HCDI (~ 35 mg g^{-1} in 6 g L^{-1}) (Lee, Kim et al. 2014, Kim, Lee et al. 2016). A primary reason for this superior desalination performance is attributed to the nature of this hybrid system.

50

Because an oxidation process was utilized as a counterpart of the desalination system, the anions were deionized by spontaneous diffusion into the oxidation cell without employing the anode for capturing the anions. The desalination capacity was estimated by following Equation (2):

$$\frac{1}{C_{Desalination}} = \frac{1}{(C_{Cations} + C_{Diffusion})/m_{Cathode}} \qquad (2)$$

where $C_{Desalination}$ is the desalination capacity of the system, $C_{Cations}$ is the capacity of deionized cations, $C_{Diffusion}$ is the capacity of diffused anions, and $m_{Cathode}$ is the mass of the cathode employed for capturing cations. Hence, this hybrid system is able to achieve desalination performance twice as high as the conventional system that consists of a cathode and anode, which is estimated by following Equation (3):

$$\frac{1}{C_{Desalination}} = \frac{1}{C_{Cations}/m_{Cathode}} + \frac{1}{C_{Anions}/m_{Anode}} \qquad (3)$$

where $C_{Desalination}$, $C_{Cations}$ and $m_{Cathode}$ are have a corresponding meaning in Equation (2), C_{Anions} is the capacity of deionized anions, and m_{Anode} is the mass of the anode employed for capturing anions. In addition, utilizing an oxidation process demonstrated a new embodiment of an electrochemical desalination system without employing the anode for capturing anions.   This provides an opportunity to overcome the limitations associated with selecting materials for anion capture.

Figure 3-5 (c) presents the correlation ($R^2 = 0.99$) between the specific capacity of the $Na_{0.44}MnO_2$ (Figure 3-5 (a)) and its desalination capacity (Figure 3-5 (b)) with high average efficiency of approximately 98%. This high efficiency implies that this hybrid system makes full use of the specific capacity of the electrode independently of electrolyte concentration. Note that the efficiency in each concentration of NaCl was calculated by total consumed coulombs for deionized NaCl (Figure 3-5 (b)) per the specific capacity of the $Na_{0.44}MnO_2$ (Figure 3-5 (a)).

(a)

(b)
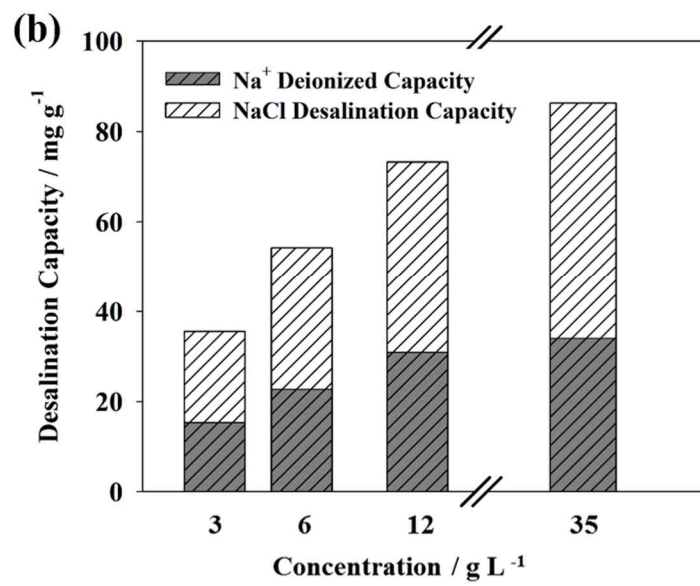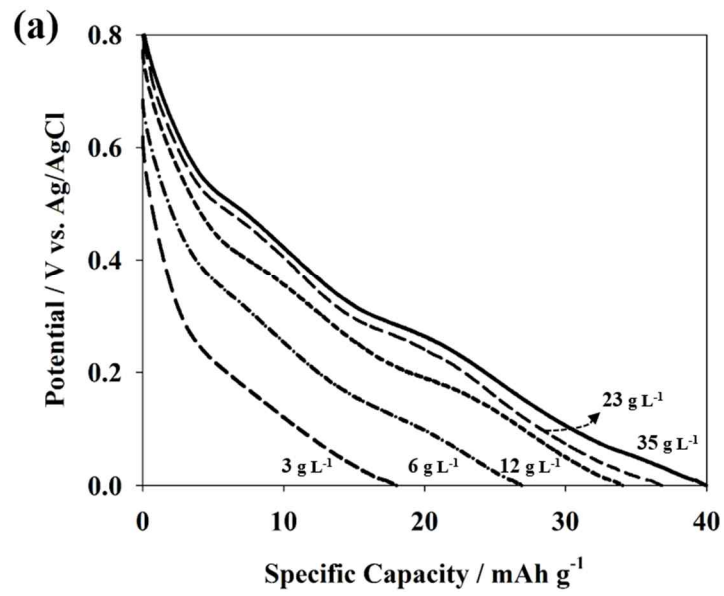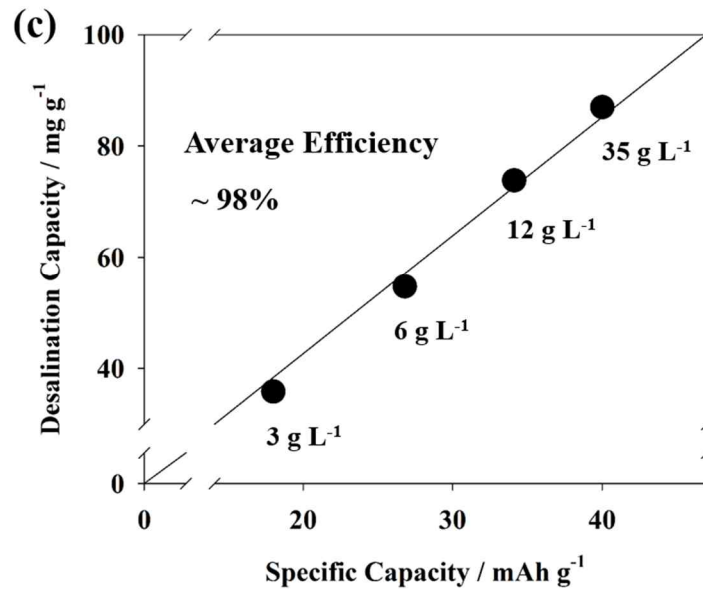
Figure 3-5. (a) Discharging curves and (b) desalination capacity of the Na$_{0.44}$MnO$_2$ in the range of 3 g L^{-1} to 35 g L^{-1} NaCl (The current density: 1C, 50 mA g^{-1} based on the Na$_{0.44}$MnO$_2$), and (c) the correlation between specific capacity of the Na$_{0.44}$MnO$_2$ and desalination capacity of the hybrid electrochemical water treatment system.

Figure 3-6 (a) and (b) show the coulombic efficiency of chlorine generation of the m-Blue TiO_2 NTs in comparison with that of the IrO_2/Ti electrode at two conditions of 35 g L^{-1} and 3 g L^{-1} of NaCl, respectively. Note that the IrO_2/Ti electrode was selected due to its popular application for chlorine generation, and an identical current density was applied to the m-Blue TiO_2 NTs and IrO_2/Ti electrode (3.5 mA cm^{-2}). As shown in Figure 3-6 (a) and (b), the efficiency of chlorine generation on the m-Blue TiO_2 NTs was higher than that on the IrO_2/Ti electrode. For instance, in the condition of 35 g L^{-1}, the coulombic efficiency of the m-Blue TiO_2 NTs for chlorine efficiency was approximately 80% ~ 95%, while that of the IrO_2/Ti electrode was approximately 65% ~ 90%. This difference was larger at a lower concentration of NaCl (3 g L^{-1}). The efficiency of the m-Blue TiO_2 NTs was maintained at approximately 70% ~ 80%, whereas that of the IrO_2/Ti electrode was only 45% in 3 g L^{-1}. The high efficiency of the m-Blue TiO_2 NTs for chlorine generation is consistent with the result in the oxidation cell in Table 3-1.
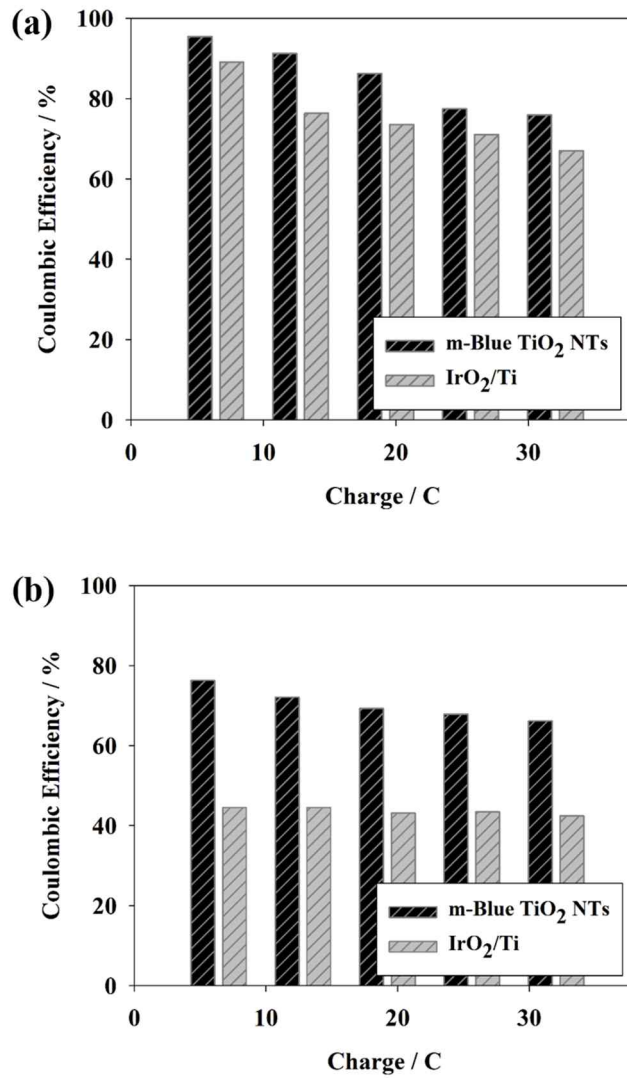
Figure 3-6. The coulombic efficiency of the m-Blue TiO$_2$ NTs for chlorine generation in comparison with that of the IrO$_2$/Ti electrode at two conditions (a) the 35 g L^{-1} and (b) 3 g L^{-1} of NaCl (current density: 3.5 mA cm^{-2}).

Figure 3-7 (a) and (b) show the FE-SEM images of the m-Blue TiO_2 NTs as an oxidant generation anode and the $Na_{0.44}MnO_2$ as a cation-capturing cathode in the hybrid system, respectively. As shown in the top-view images in Figure 3-7 (a), TiO_2 NTs grown via electrochemical anodization appeared to be highly ordered. The outer diameter of the m-Blue TiO_2 NTs was approximately 100 nm, and the wall thickness was 20 nm. The length of the m-Blue TiO_2 NTs was approximately 15 μm. The high efficiency of chlorine generation on the m-Blue TiO_2 NTs in Figure 3-6 (a) and (b) could be attributed to its well-organized nanotube structure (Figure 3-7 (a) and Figure 3-8) or its intrinsic properties (e.g., affinity for oxygen, working potential and over potential), which allows for the efficient mass transfer of chloride ions from the bulk to the interface. In addition, $Na_{0.44}MnO_2$, exhibiting a mean diameter of approximately 300 nm and a length of $1 - 2$ μm, is presented in Figure 3-7 (b).
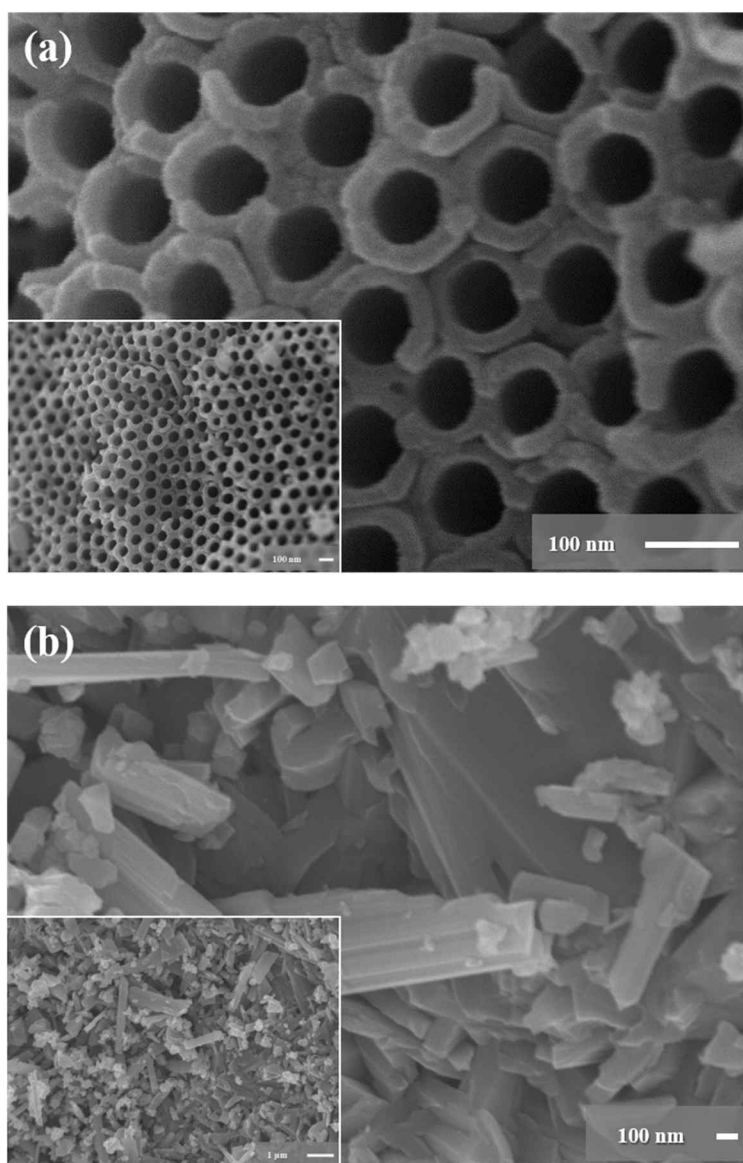
Figure 3-7. The FE-SEM images of (a) the m-Blue TiO_2 NTs as the oxidant generation anode and (b) the $Na_{0.44}MnO_2$ as the cation capturing cathode in the hybrid electrochemical water treatment system.

58

Figure 3-8 (a) and (b) presents the top-view and side-view FE-SEM images of the m-Blue TiO_2 NTs, respectively. As shown in Figure 3-8 (a) and (b), the thickness of one strand of meshed Ti was approximately 400 μm. TiO_2 nanotubes of approximately 15 μm were grown on the Ti substrate. Figure 3-8 (c) shows the anodized TiO_2 nanotube on meshed Ti substrate (amorphous phase, on left) and the m-Blue TiO_2 NTs (anatase phase, on right). After the annealing and cathodic polarization treatment, the anodized TiO_2 nanotube was changed from a yellow color to blue color, leading to the activation the electro-catalyst as an oxidant generation anode.
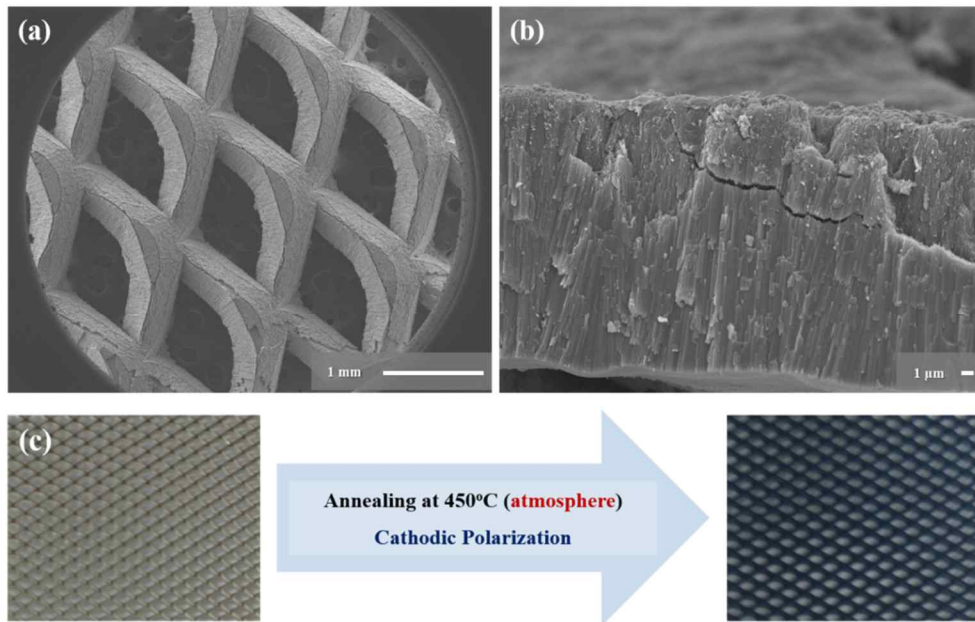
Figure 3-8. (a) Top-view and (b) side-view FE-SEM images of m-Blue TiO$_2$ NTs, and (c) fabricating scheme of the m-Blue TiO$_2$ NTs, anodized TiO$_2$ nanotube on meshed Ti substrate (left) and Blue TiO$_2$ NTs (right), treated by annealing and cathodic polarization.

60

Figure 3-9 (a) and (b) present the electrochemical characteristics of the $Na_{0.44}MnO_2$ analyzed via CV and galvanostatic charge/discharge, respectively. As shown in Figure 3-9 (a), four distinct peaks of the intercalation (0.07, 0.16. 0.31 and 0.55 V) and de-intercalation (0.22, 0.27, 0.46 and 0.67 V) of sodium ions with the $Na_{0.44}MnO_2$ were observed between 0 V and 0.8 V (vs. Ag/AgCl KCl sat'd). Moreover, the plateaus at the potential corresponding to peaks in CV were consistently exhibited in the charging and discharging in Figure 3-9 (b). This implies that the $Na_{0.44}MnO_2$ offers four different sites involving intercalation and de-intercalation of sodium ions. Despite the theoretical possibility of the oxygen evolution reaction over 0.6 V (vs. Ag/AgCl KCl sat'd) at a neutral pH, the $Na_{0.44}MnO_2$ demonstrated coulombic efficiency of approximately 99% by suppressing oxygen evolution due to its high over-potential. Within the potential range, the $Na_{0.44}MnO_2$ showed high specific capacity and rate capability. For instance, the specific capacity of approximately 47 mAh g^{-1} was measured at 50 mA g^{-1} (1 C based on the theoretical specific capacity: ~ 50 mAh g^{-1}). Furthermore, Figure 3-9 (c) shows the rate capability of a $Na_{0.44}MnO_2$ measured at 1 C for charging and at various rates for discharging. As shown in Figure 3-9 (c), the $Na_{0.44}MnO_2$ exhibited good rate capability. For instance, the specific capacity of approximately 47 mAh g^{-1} was measured at 50 mA g^{-}

^{1} (1 C based on the theoretical specific capacity: ~ 50 mAh g^{-1}). Furthermore, approximately 90% and 80% of the specific capacity was retained at 3/2 C and 2 C, respectively.

63
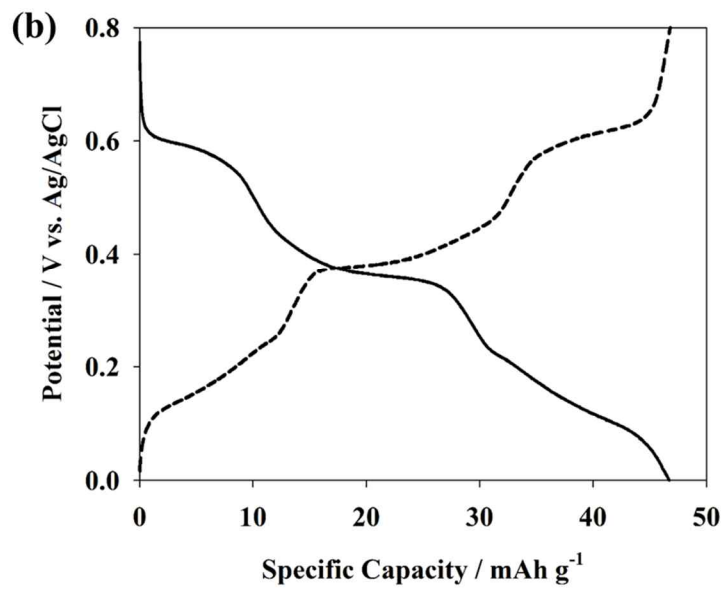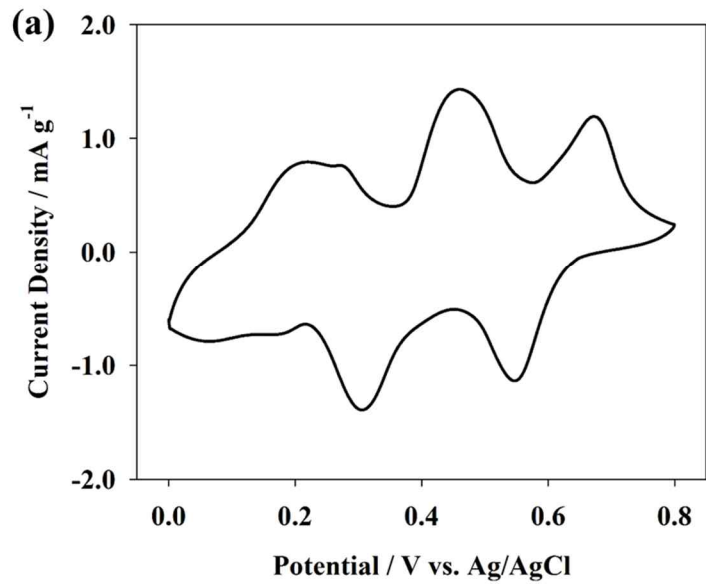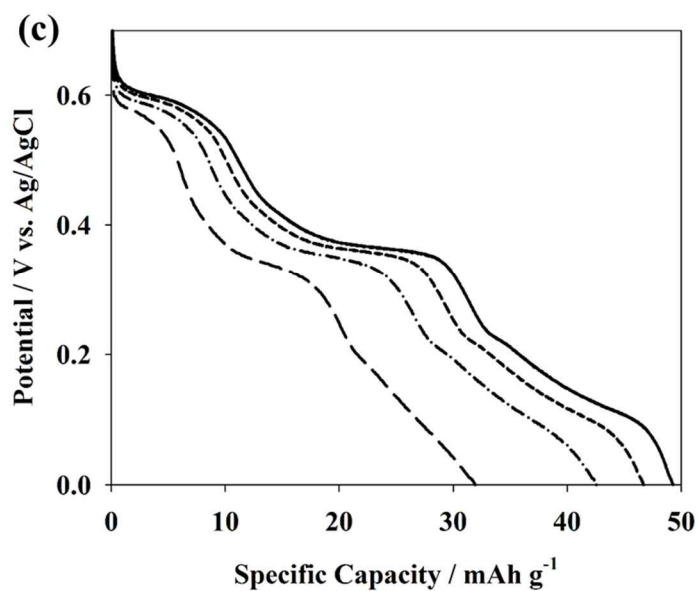
Figure 3-9. (a) CV, (b) galvanostatic charge/discharge and (c) Discharging curves of $Na_{0.44}MnO_2$ in 3.5 M of NaCl electrolyte. CV was conducted in at a scan rate of 2 mV s^{-1}. Galvanostatic charge/discharge was measured by the current density of 50 mA g^{-1}. The current density was varied from 25 mA g^{-1} to 100 mA g^{-1} in discharging curves.

Figure 3-10 (a) and (b) present the HR-XRD patterns of the m-Blue TiO_2 NTs and the $Na_{0.44}MnO_2$, respectively. As shown in Figure 3-10 (a), the patterns exhibited diffraction peaks at 25.3°, 37.8°, 53.9° and 55.1°, indicating TiO_2 in the anatase phase. In Figure 3-10 (b), the peaks at 19.5°, 34.1°, 37.4°, and 51.5° were exhibited, indicating $Na_{0.44}MnO_2$ with orthorhombic structure. All peaks are in agreement with the standard spectrum (JCPDS no. 84-1285 (TiO_2) and 27-0750 ($Na_{0.44}MnO_2$)).
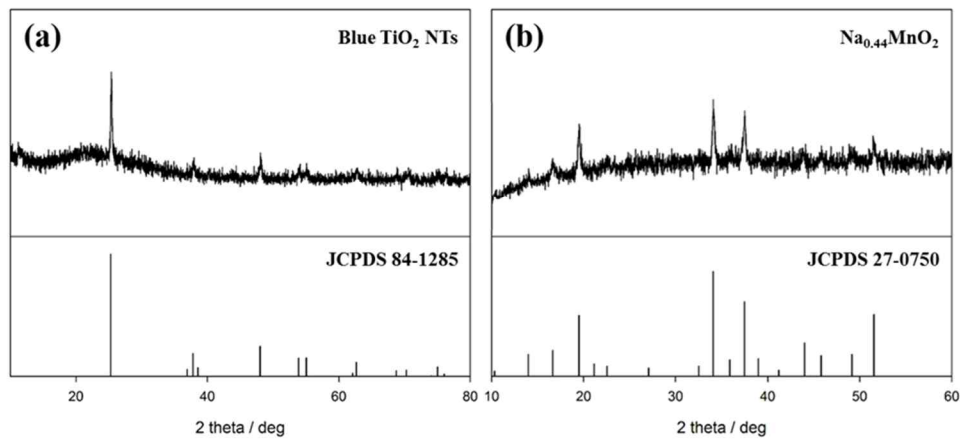
Figure 3-10. HR-XRD patterns of (a) the m-Blue TiO_2 NTs and (b) the $Na_{0.44}MnO_2$ and standard spectrum of TiO_2 (a) and $Na_{0.44}MnO_2$ (b).

3.4.   Summary

In this study, a novel hybrid electrochemical water treatment system combining an electrochemical desalination system with an oxidation process was successfully demonstrated by intercalation of cations on a cathode, spontaneous diffusion of anions through the anion exchange membrane and the simultaneous reaction of chlorine generation. As a primary result, superior desalination capacities of approximately 87 mg g^{-1} and 36 mg g^{-1} were achieved in 35 g L^{-1} and 3 g L^{-1} NaCl, respectively. In addition, this hybrid system showed a coulombic efficiency of approximately 98% and 66% in synthetic brackish water for desalination and oxidation, respectively. The m-Blue TiO$_2$ NT as an anode electrode functions efficiently for chlorine generation, even in low concentrations of electrolyte. Consequently, by combining the desalination process and the oxidation process, this hybrid system showed superior desalination capacity and efficiency, and it provided a new strategy to overcome the limitations of materials used for capturing anions.

4. Na$_2$FeP$_2$O$_7$ as Novel Material for Hybrid Capacitive Deionization

4.1. Introduction

Various novel CDI systems were investigated, including flow-through electrode capacitive desalination (FTE CD), ion exchange membrane assisted CDI (MCDI) and ion exchange resin coated CDI, Flow-electrode capacitive deionization (FCDI), inverted CDI (*i*-CDI) and desalination battery system (Lee, Park et al. 2006, Biesheuvel and Van der Wal 2010, Kim and Choi 2010, La Mantia, Pasta et al. 2011, Pasta, Wessells et al. 2012, Suss, Baumann et al. 2012, Jeon, Park et al. 2013, Gao, Omosebi et al. 2014, Jeon, Yeo et al. 2014, Porada, Weingarth et al. 2014, Gao, Omosebi et al. 2015, Gao, Omosebi et al. 2015). A recently introduced Hybrid CDI (HCDI), which utilizes sodium manganese oxide (Na$_4$Mn$_9$O$_{18}$), a representative material for sodium ion batteries (SIBs), to replace one of the carbon electrodes, successfully demonstrated its superior deionization performance (31.2 mg of NaCl per g of electrodes) over conventional CDI (Lee, Kim et al. 2014).

As shown in Figure 4-1, in the HCDI system, sodium ions are intercalated on the sodium manganese oxide electrode and chloride ions are adsorbed on the activated carbon electrode, leading to a deionization process. Alternatively, the captured sodium and chloride ions are released from the sodium manganese oxide and activated carbon electrodes, respectively, during the discharge step. Despite the great promise of the HCDI system, the limited availability of aqueous-based intercalation materials and the lack of information regarding the characteristics of the HCDI system performance are obstacles to the advancement of HCDI to compete with reverse osmosis for deionization.

This study attempted to investigate the overall kinetic deionization performance of HCDI with sodium iron pyrophosphate ($Na_2FeP_2O_7$). It has been noted that among the various materials for SIBs that have been used in large-scale energy storage systems (ESSs) as an alternative to grid energy storage, $Na_2FeP_2O_7$ is attractive due to it high capacity, stability, low cost and environmentally benign nature (Kim, Shakoor et al. 2013, Chen, Matsumoto et al. 2014, Jung, Lim et al. 2014, Kim, Hong et al. 2014). In addition, the analysis of the CDI Ragone plot was applied to investigate the operational behavior of the HCDI system with $Na_2FeP_2O_7$ combined with a battery and supercapacitor compared to the conventional MCDI system.

69
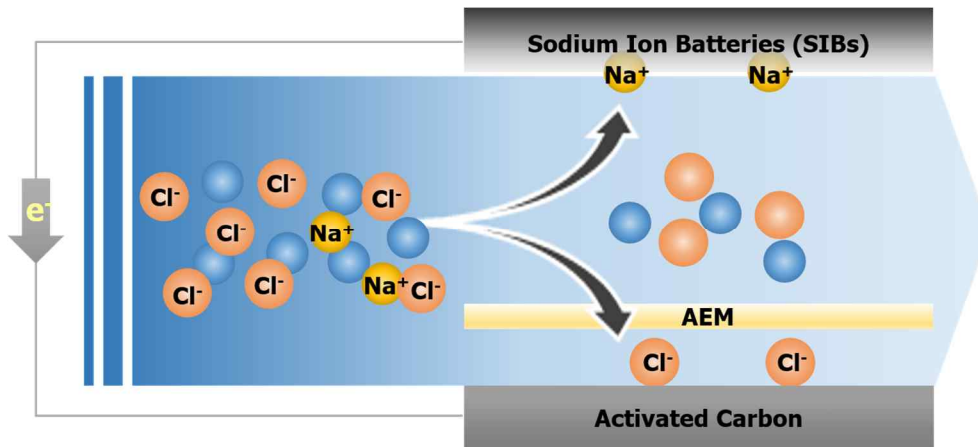
Figure 4-1. Scheme of Hybrid CDI (HCDI) consisting of sodium ion batteries (SIBs) on one side of the electrode instead of carbon material as well as an anion exchange membrane assisted activated carbon (AC). During the charging process, sodium ions are intercalated onto the SIB and chloride ions are absorbed onto the AC.

4.2.   Experimental

4.2.1.   Material synthesis

Sodium iron pyrophosphate was synthesized via a solid-state reaction with Na_2CO_3, $(NH_4)_2HPO_4$, and FeC_2O_4 (Sigma Aldrich) following the procedure reported in a previous study (Kim, Shakoor et al. 2013). These chemicals were mildly mixed at a molar ratio of 1: 2: 1 ($NaCO_3$, $(NH_4)_2HPO_4$, and FeC_2O_4). Then, the mixed powder was pelletized and annealed at 350°C for 3 h under an inert atmosphere and cooled to room temperature. The product was re-pelletized and annealed at 600°C for 6 h under a N_2 atmosphere. To enhance the electrical conductivity, the prepared powder was ball-milled and carbon-coated with carbon black at a weight ratio of 8: 2 (prepared powder: Super P). The carbon coated powder was pelletized and annealed at 600°C for 10 h under a N_2 atmosphere. The prepared material was characterized by scanning electron microscopy (SEM), energy-dispersive X-ray spectroscopy (EDS, JEOL JSM 6700F) and inductively coupled plasma atomic emission spectroscopy (ICP-AES, Optima-4300 DV, PerkinElmer). The crystalline structure was analyzed by X-ray powder diffraction (XRD, Bruker D8 DISCOVER).

4.2.2. Electrode fabrication

The $Na_2FeP_2O_7$ electrode employed in the HCDI system was fabricated by a slurry mixture of its powder (75 wt%), carbon black (Super P, Timkan graphite and carbon 15 wt%) and polytetrafluoroethylene (PTFE, Sigma-Aldrich, 10 wt%). The activated carbon electrode was also prepared by a slurry mixture of carbon powder (MSP-20, Kansai Coke and Chemicals, 86 wt%), Super P (7 wt%) and PTFE (7 wt%). Slurry mixtures were treated with a roll press machine to fabricate the sheet-type electrodes with an approximate thickness of 300 μm. The electrodes were dried in a vacuum oven at 60°C for 12 h to remove the remaining solvent.

4.2.3. Electrochemical characterization

Cyclic voltammetry (CV) was carried out with a potentiostat (PARSTAT 2273, Princeton Applied Research) using a three electrodes system in an aqueous 2 M NaCl electrolyte. The system consisted of $Na_2FeP_2O_7$ for the working electrode, excess activated carbon for the counter electrode, and KCl saturated Ag/AgCl for the reference electrode. Galvanostatic charge/discharge, cycling and rate capability were conducted by $Na_2FeP_2O_7$ and an activated carbon system using a battery cycler (WBCS3000, WonA Tech Co) in an aqueous 2 M NaCl electrolyte. A cellulose nitrate membrane (Advanced Microdevice, thickness ~ 110 μm) was used as a separator between the two electrodes.

4.2.4. Deionization test

The deionization performance, following the procedure of the previous studies from our group, was conducted in a continuous flow system with a pair of 2-cm diameter electrodes, a 200-μm thick nylon spacer and an anion exchange membrane (AMV, AGC engineering Co.) (Kim, Lee et al. 2014, Lee, Kim et al. 2014, Kim and Yoon 2015). The contact area of two electrodes was 3 cm^2 due to the flow stream. Before installation of the electrode, the electrode was treated with a pre-charging process in which a potential of 0.6 V (vs. Ag/AgCl) was applied for 30 min to the $Na_2FeP_2O_7$ electrode, leading to Na defect sites in $Na_2FeP_2O_7$. Under constant voltage operations, 1.2 V and -1.2 V were applied to the HCDI cell for 15 min for the charging and discharging process, respectively. Under constant current, the current densities varied from 60 mA g^{-1} to 180 mA g^{-1} (1 mA^{-2} to 3 mA cm^{-2}) based on the $Na_2FeP_2O_7$ electrode using the battery cycler. The flow rate was 2 mL min^{-1}, and the feed water contained 10 mM, 50 mM and 100 mM of NaCl. The feed concentration was measured by a conductivity meter (3573-10C, HORIBA, Ltd). The deionization performance was expressed as the mass of deionized NaCl salt per $Na_2FeP_2O_7$. In CDI, the performance of deionization is typically evaluated in terms of the salt adsorption capacity, maximum salt adsorption rate and average salt adsorption rate (ASAR) (Porada, Borchardt

et al. 2013, Zhao, Satpradit et al. 2013). Since sodium ions are captured by the intercalation reaction, the parameters for evaluating the deionization performance are denoted by the deionization capacity, maximum deionization rate and average deionization rate in HCDI. All experiments were carried out in duplicate or triplicate to examine their reproducibility.

4.3.   Results and Discussion

Figure 4-2 (a) provides XRD data of $Na_2FeP_2O_7$ and the Rietveld refinement pattern based on $Na_2CoP_2O_7$-rose, adopting a triclinic structure under the P1 space group. As seen in Figure 4-2 (a), the XRD pattern fit well with that of $Na_2CoP_2O_7$-rose, which indicates that $Na_2FeP_2O_7$ possesses a highly crystallized structure with a pure phase and infinite metal polyhedrals and pyrophosphate groups connected with shared corners utilizing the migration of Na ions (Erragh, Boukhari et al. 1991, Kim, Shakoor et al. 2013). The lattice parameters were analogous to those of $Na_2FeP_2O_7$ reported in a previous study (a = 9.71 Å, b = 11.01 Å, c = 12.32 Å, α = 148.62°, β = 121.67° and γ = 68.43°) (Kim, Shakoor et al. 2013). As shown in Figure 4-2 (b) and (c), the mixed powders before ball-milling and carbon coating showed particle sizes of 10 to 50 μm and rocklike shapes. After ball-milling and the carbon coating treatment, the particles were smashed to small pieces that were sub-micron sized.
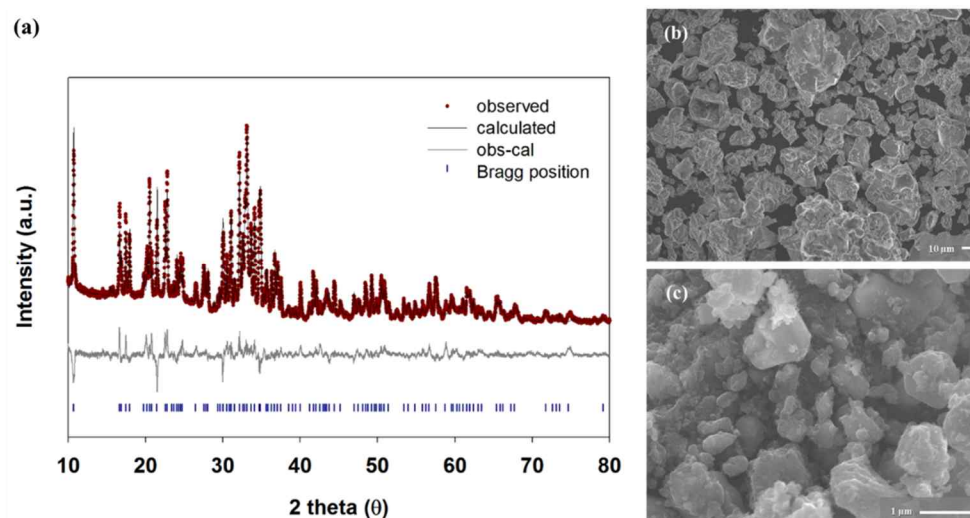
Figure 4-2. (a) XRD data of $Na_2FeP_2O_7$ and the Rietveld refinement pattern based on $Na_2CoP_2O_7$-rose, adopting a triclinic structure under the P1 space group (Rp = 9.40%, Rwp = 7.15%, χ^2 = 4.01). Observed and calculated data are presented as red markers and the black line, respectively. The gray line and blue bars indicate the differences in the fitting residual and Bragg positions, respectively. SEM images of $Na_2FeP_2O_7$ powders synthesized by a solid state reaction (b) before carbon coating and (c) after carbon coating and ball-milling.

Figure. 4-3 shows the EDS mapping scanning spectra (a) for sodium (Na), iron (Fe), phosphor (P) and oxygen (O) consisting of the $Na_2FeP_2O_7$ and the SEM image of $Na_2FeP_2O_7$ powders. As shown in 4-3, through EDS mapping scanning spectra of the $Na_2FeP_2O_7$, for Na, Fe, P, and O, were uniformly distributed on the whole surface of prepared powder. The stoichiometry of $Na_2FeP_2O_7$ for Na, Fe and P was confirmed as 2 : 1 : 2 based on the results of ICP-AES (1.97 : 1.05 : 2) and SEM-EDS (1.96 : 0.99 : 2) analyses.
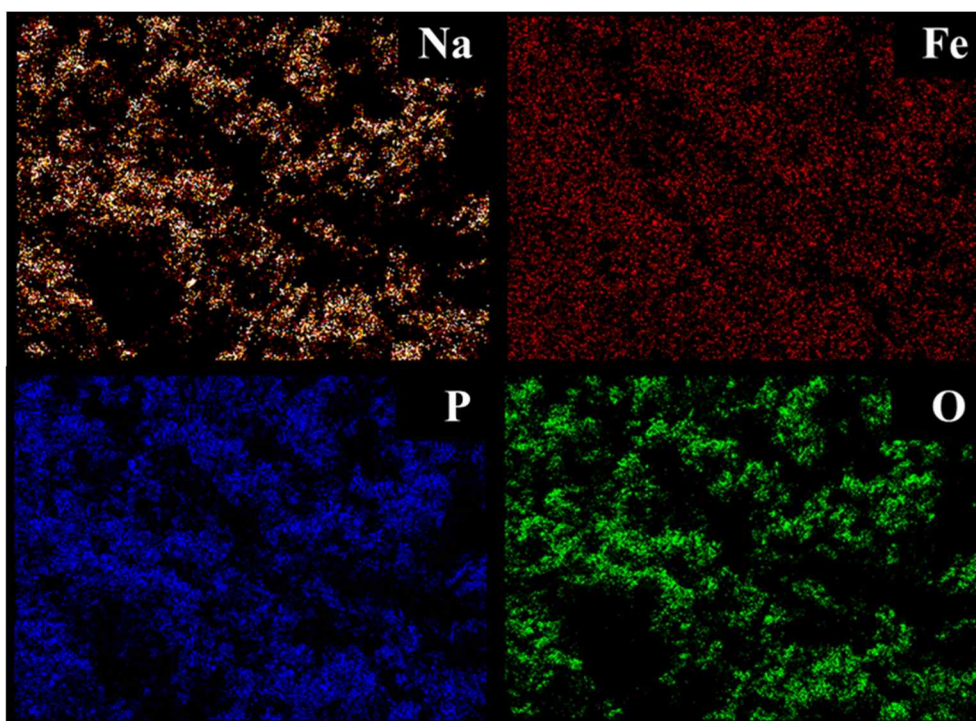
Figure 4-3. EDS mapping scanning spectra of $Na_2FeP_2O_7$ for sodium (Na), iron (Fe), phosphorus (P) and oxygen (O).

Figure 4-4 (a) and (b) show the electrochemical characterization of $Na_2FeP_2O_7$ as measured by CV and galvanostatic charge/discharge, respectively. In Figure 4-4 (a), the characteristic peaks related to the de-intercalation and intercalation reactions of sodium ions with $Na_2FeP_2O_7$ were observed at -0.36, 0.07, 0.18 and 0.43 V (black arrows) and -0.45, -0.07, 0.06 and 0.41 V (gray arrows), respectively, based on the Ag/AgCl KCl saturated electrode, suggesting that de-intercalation and intercalation reactions of sodium ions with $Na_2FeP_2O_7$ occurred over the potential range preventing electrolysis at a neutral pH and were consistent with the literature values (Kim, Shakoor et al. 2013, Jung, Lim et al. 2014). In galvanostatic charge/discharge (Figure 4-4 (b)), the capacity of $Na_2FeP_2O_7$ was shown to be approximately 56 mAh g^{-1} at 48 mA g^{-1} (1/2 C based on the theoretical capacity: 97 mAh g^{-1}).(Kim, Shakoor et al. 2013) This capacity corresponded to approximately 200 F/g of capacitance, which was a much higher value than that of conventional activated carbon materials (~130 F g^{-1} of MSP 20 in 1 M of NaCl).(Kim and Yoon 2013) More than 97% of the capacity was retained for 120 cycles at a current density of 384 mA g^{-1} (Figure 4-5), demonstrating that there is good capacity retention in the HCDI system under aqueous conditions.
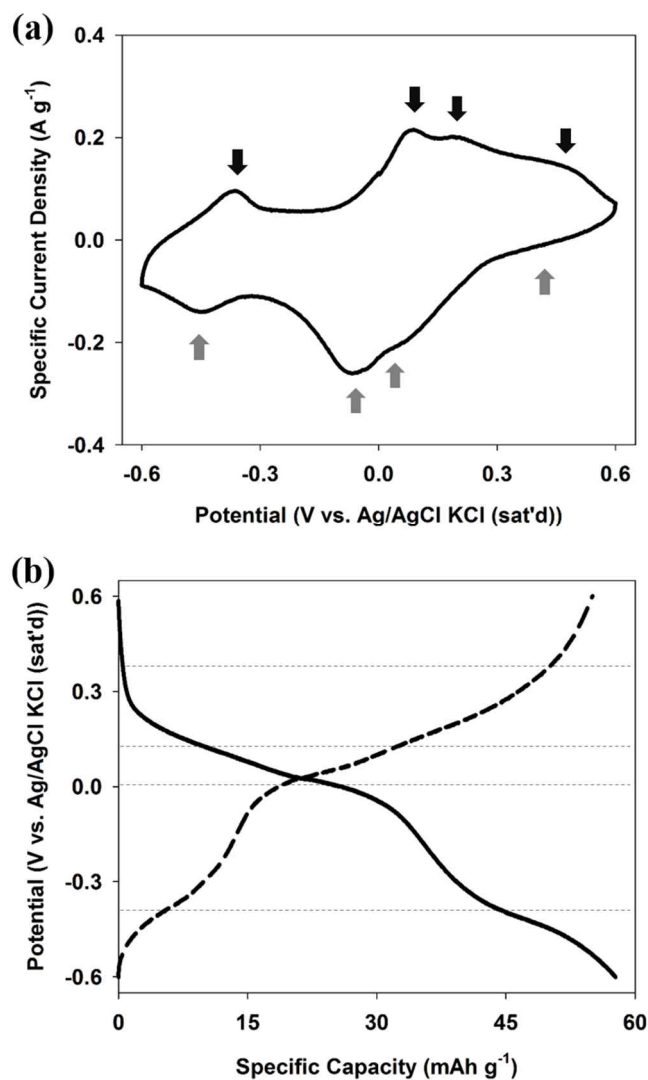
Figure 4-4. The representative characterization of the (a) CV and (b) galvanostatic charge/discharge of $Na_2FeP_2O_7$ in 2 M of NaCl (pH ~ 7). CV was carried out at a scan rate of 0.5 mV s^{-1}. Galvanostatic charge/discharge was conducted with a current density of 48 mA g^{-1}.

Figure. 4-5 presents the galvanostatic charge and discharge capacity retention of HCDI system with $Na_2FeP_2O_7$ up to 120 cycles at two specific current densities of 192 mA/g and 384 mA/g (corresponding to current density as 2C and 4C based on theoretical capacity of $Na_2FeP_2O_7$). As shown in Figure. 4-5, over 94% and 97% of capacity was retained for 120 cycles at current density of 192 mA/g and 384 mAh/g, respectively.
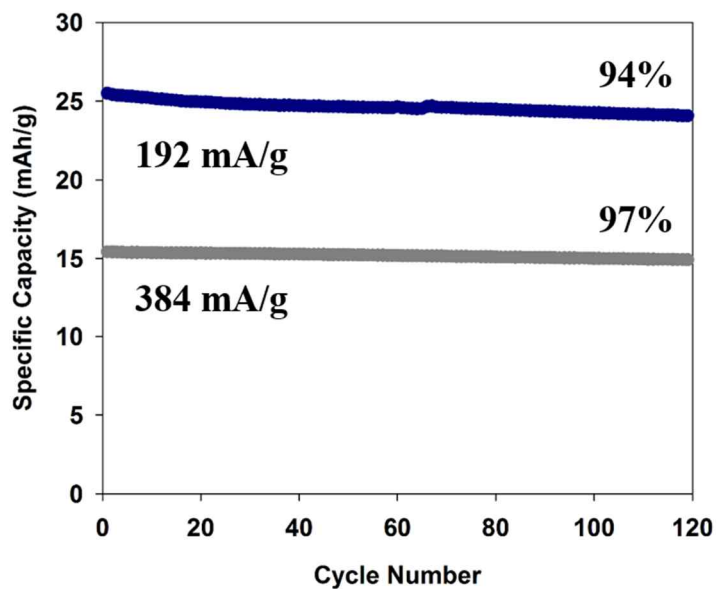
Figure 4-5. The retention of the charge and discharge capacity of the HCDI system with $Na_2FeP_2O_7$ with the cycle number (two specific current densities of 192 mA g^{-1} and 384 mA g^{-1} with a potential window of -0.6 V to 0.6 V based on the Ag/AgCl KCl saturated electrode).

Figure 4-6 shows the deionization characteristics of the HCDI system with Na$_2$FeP$_2$O$_7$ in terms of (a) the conductivity profile of the effluent, (b) the current (solid line) vs. the voltage profile (dotted line) of the HCDI system under constant voltage operations and (c) the deionization capacity (mg g^{-1}) and average deionization rate (mg g^{-1} s^{-1}). As shown in Figures 4-6 (a) and 4(b), the HCDI system exhibited the typical deionization behavior of the CDI system under constant voltage operation. For instance, the conductivity of the effluent rapidly decreased initially during the charging process, triggered by the instant change in the electric energy state between the two electrodes. As the system reached the equilibrium state where ions can no longer be removed, the conductivity of the effluent recovered to the initial value. On the other hand, the effluent conductivity increased when the captured ions were released during the discharge process, in which the system can be regenerated.

Figure 4-6 (c) shows that the HCDI system with $Na_2FeP_2O_7$ has a superior deionization rate performance compared to the CDI system, the MCDI system, and even the previous HCDI system with $Na_4Mn_9O_{18}$ reported by previous study (Lee, Kim et al. 2014). For instance, the maximum deionization rate of the HCDI system with $Na_2FeP_2O_7$ was 0.081 mg g^{-1} s^{-1}, which is approximately 69%, 13%, and 23% faster than those of the previously listed CDI systems, respectively. In addition, the deionization capacity of HCDI with $Na_2FeP_2O_7$ (30.2 mg g^{-1}) was higher than that of the CDI (13.5 mg g^{-1}) and MCDI systems (22.4 mg g^{-1}), with higher capacity for $Na_2FeP_2O_7$ than for carbon material. However, no significant difference in the deionization capacity between the two HCDI systems with $Na_2FeP_2O_7$ and $Na_4Mn_9O_{18}$ (31.2 mg g^{-1}) were observed. This is explained by the fact that the deionization capacity of the HCDI system is limited by the relatively low capacity of the carbon material.
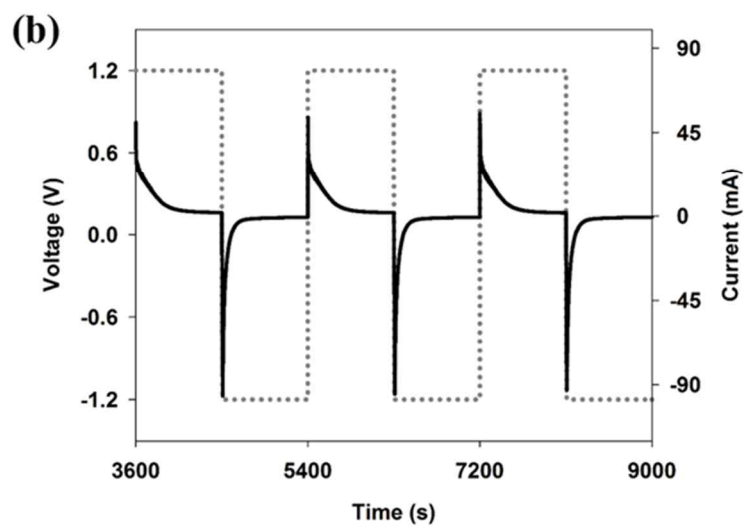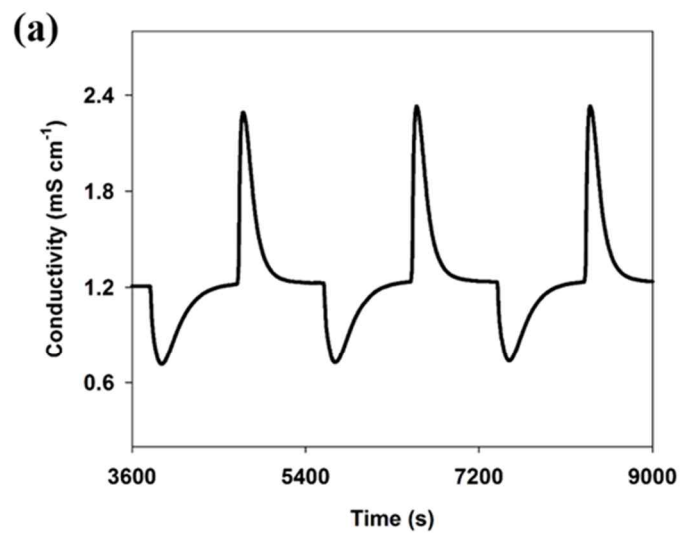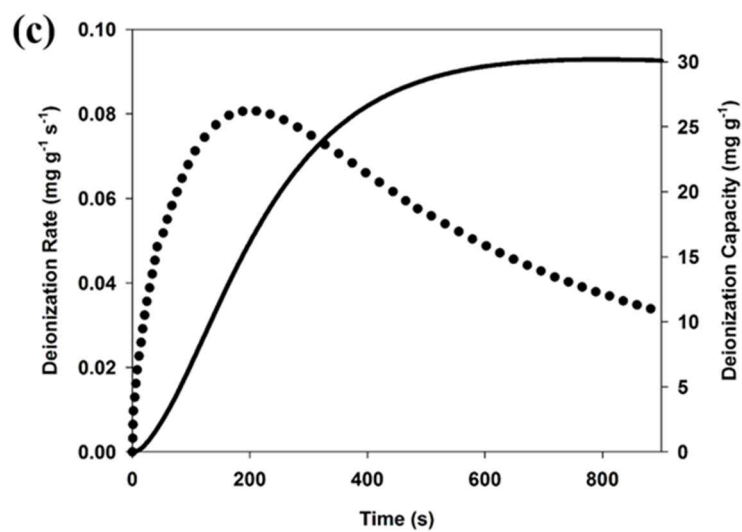
Figure 4-6. The (a) effluent conductivity profile and (b) current-voltage profile of the HCDI system under constant voltage operation and (c) the deionization capacity and rate during the charging step. Positive and negative 1.2 V of cell voltage were applied for 15 min during the charging and discharging processes, respectively, and the influent was 10 mM NaCl.

87

Figure 4-6 compares the normalized deionization capacity to the maximum deionization rate of the HCDI system with respect to the influent concentration (10, 50 and 100 mM of NaCl) and constant voltage operations (0.9, 1.2 and 1.5 V). Note that the data were calculated based on the results at 100 mM and 1.2 V (deionization capacity: 32.6 mg g-1, maximum deionization: 0.143 mg g^{-1} s^{-1}), and the results from Figure 4-5 (c) (10 mM & 1.2 V) were included for comparative purposes. As shown in Figure 4-6, the increase in both the influent concentration and operation voltage contributed to the enhanced deionization capacity and maximum deionization rates, although the effect differs to some extent. For instance, the deionization capacity at 1.2 V (30 ~ 33 mg g^{-1}) did not change much regardless of the influent concentration, indicating that this HCDI system was near the equilibrium state. However, the maximum deionization rate under this condition is variable with changing influent concentrations. The deionization rate was 40% higher at 100 mM than at 10 mM and 50 mM, implying that the influent concentration influences the deionization rate due to the kinetic accessibility of the ionic species on the surface of the electrodes. A high influent concentration induces the facilitated transport of ions by reducing the ionic resistance in the electrolytes, resulting in the enhancement of the deionization rate.

88
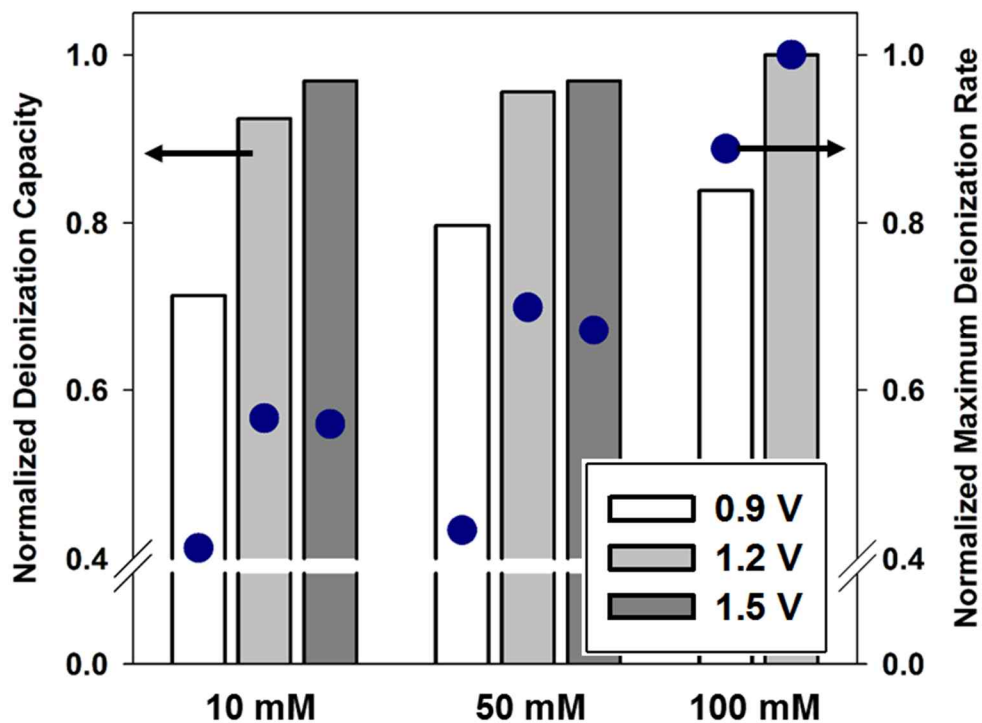
Figure 4-7. Comparison of the normalized deionization capacity to the maximum deionization rate of the HCDI system with respect to the influent concentration (10, 50 and 100 mM of NaCl) under constant voltage (0.9, 1.2 and 1.5 V). Note that the data are calculated based on the results at 100 mM and 1.2 V (deionization capacity: 32.6 mg g^{-1}, maximum deionization: 0.143 mg g^{-1} s^{-1}), and the results from Figure 4-5 (c) (10 mM and 1.2 V) are included for comparative purposes.

Figures 4-7 (a) and (b) represents (a) three consecutive cycles of the effluent conductivity profiles and (b) the current (dotted line, 1 mA cm^{-2}) vs. voltage (solid line) profile of the HCDI system with $Na_2FeP_2O_7$ under a constant current. The deionization behaviors under a constant current shown in Figures 4-7 (a) and (b) are distinguished from those under a constant voltage (Figures 4-5 (a) and (b)). For instance, as shown in Figure 4-7 (a), the conductivity of the effluent under a constant current was retained by the current density, increasing the extent of deionization. Constant current operations are often preferred due to the benefit of a steady effluent concentration and the simplicity of the equipment for the CDI system as well as the fact that the equipment can directly connect to other electrical conversion devices (Anderson, Cudero et al. 2010). The constant current operations showed a deionization capacity of 24 mg g^{-1}, with an average deionization rate of 0.02 mg g^{-1} s^{-1}, which can be obtained from integrating Figure 6(a), indicating that the deionization capacity was 30% better for the HCDI system than the MCDI system with symmetric activated carbon (Kim and Yoon 2015).
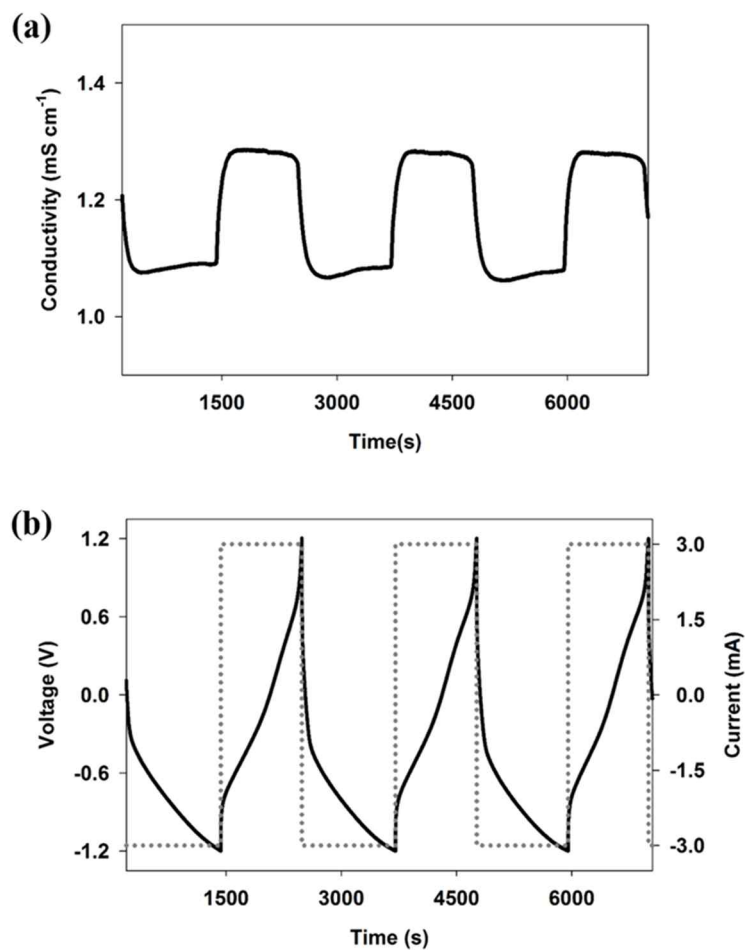
Figure 4-8. Representation of (a) three consecutive cycles of the effluent conductivity profiles and (b) the current-voltage profile of the HCDI system under a constant current. Positive and negative 1.0 mA cm^{-2} currents were applied during the charging and discharging process, respectively, with a 10 mM NaCl influent.

Figure 4-8 shows the effluent conductivity of HCDI system depending upon applied current densities (1.0, 1.5, 2.0 and 3.0 mA cm^{-2}) in 10 mM and 100 mM of NaCl, respectively. As shown in Figure 4-8, under constant current operation, the change of effluent conductivity was affected by the applied current density, allowing the extent of deionization. In Figure (a, d, e and Figure 4-7 (a)), the conductivity of effluent was stably retained at low applied current density. However, as applied current density increased, the constantly retained period of effluent conductivity was shorten (c, g), indicating the HCDI system cannot be fully showed its deionization capacity.

93
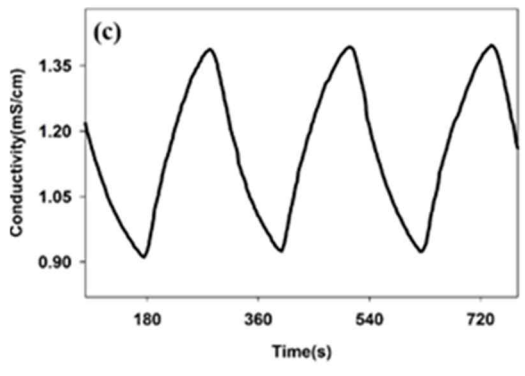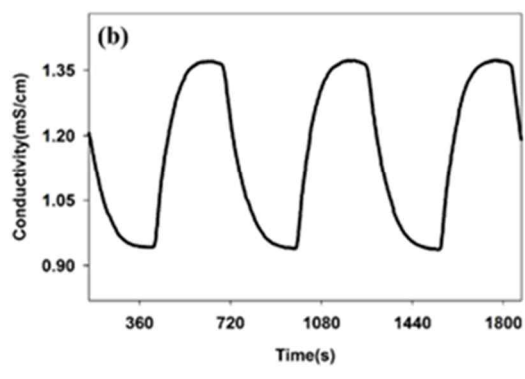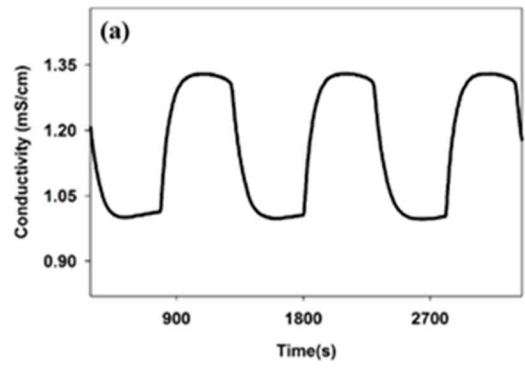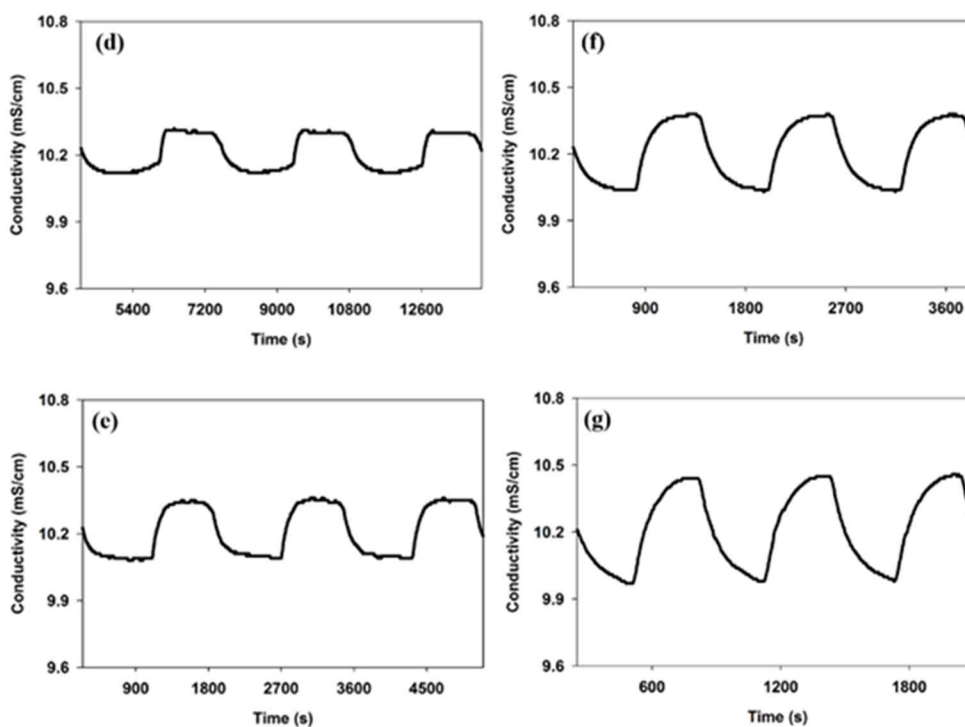
Figure 4-9. The effluent conductivity profile under a constant current at 10 mM (a, b, c) and 100 mM (d, e, f, g) NaCl. Positive and negative 1.0 (d), 1.5 (a, e), 2.0 (b, f) and 3.0 (c, g) mA cm^{-2} currents were applied during the charging and discharging process, respectively

Figure 4-9 shows the CDI Ragone plot, which describes the overall deionization performance of the HCDI system with $Na_2FeP_2O_7$ with respect to the influent concentration (10 mM and100 mM NaCl) and current density (1 mA cm^{-2}, 1.5 mA cm^{-2}, 2 mA cm^{-2} and 3 mA cm^{-2}). As shown in Figure 4-9, two important observations regarding the HCDI system, depending on the current density, can be addressed by the CDI Ragone plot.

First, at low average deionization rates (marked by green dashed box, 0.022 ~ 0.034 mg g^{-1} s^{-1}) and the corresponding low current densities (1 mA cm^{-2} or 1.5 mA cm^{-2}), the HCDI system showed a higher deionization capacity than that of the MCDI system. For instance, at an inlet concentration of 10 mM (── & ──○──), a deionization capacity of 24 mg g^{-1} was attained at an average deionization rate of 0.22 mg g^{-1} s^{-1} (current density of 1 mA cm^{-2}), which was approximately 30% higher than that in the MCDI system. This difference became more profound at higher concentrations (100 mM ──▲── & ──△──), reaching a deionized capacity that was approximately 50% higher than that in the MCDI system. The high capacity of the HCDI system (24 mg g^{-1}, 34 mg g^{-1}) originated from the battery properties of $Na_2FeP_2O_7$, which are much higher than those of activated carbon at low current densities.

95

Second, at high average deionization rates (marked by yellow dashed box, $0.05 \sim 0.07$ mg g^{-1} s^{-1}) corresponding to high current densities (2 mA cm^{-2} or 3 mA cm^{-2}), the gap in the deionization capacity between the HCDI system and MCDI system narrowed, reaching 0% (10 mM) and 20% (100 mM) at an average deionization rate of 0.06 mg g^{-1} s^{-1}. This observation showed that the capacity of Na$_2$FeP$_2$O$_7$ cannot be fully utilized at high current densities, which implies that the effect of the super-capacitive property dominated the effect of the battery power on the deionization capacity. This is further supported by the results shown in Figures 4-8 (c) and (g), which show the effluent conductivity profiles at high current densities. Overall, the results of the CDI Ragone plot in Figure 4-9 demonstrate the hybrid behavior characteristics of the HCDI system, including the high deionization capacity originating from the high capacity of Na$_2$FeP$_2$O$_7$ at low current densities and high influent concentrations as well as the fast deionization rate at high current densities and low influent concentrations. The results implied that the HCDI system is able to function as either an activated carbon based CDI or SIB based desalination depending on the operation parameters, including the current density, electrolyte concentration, resistance of system, and so on.
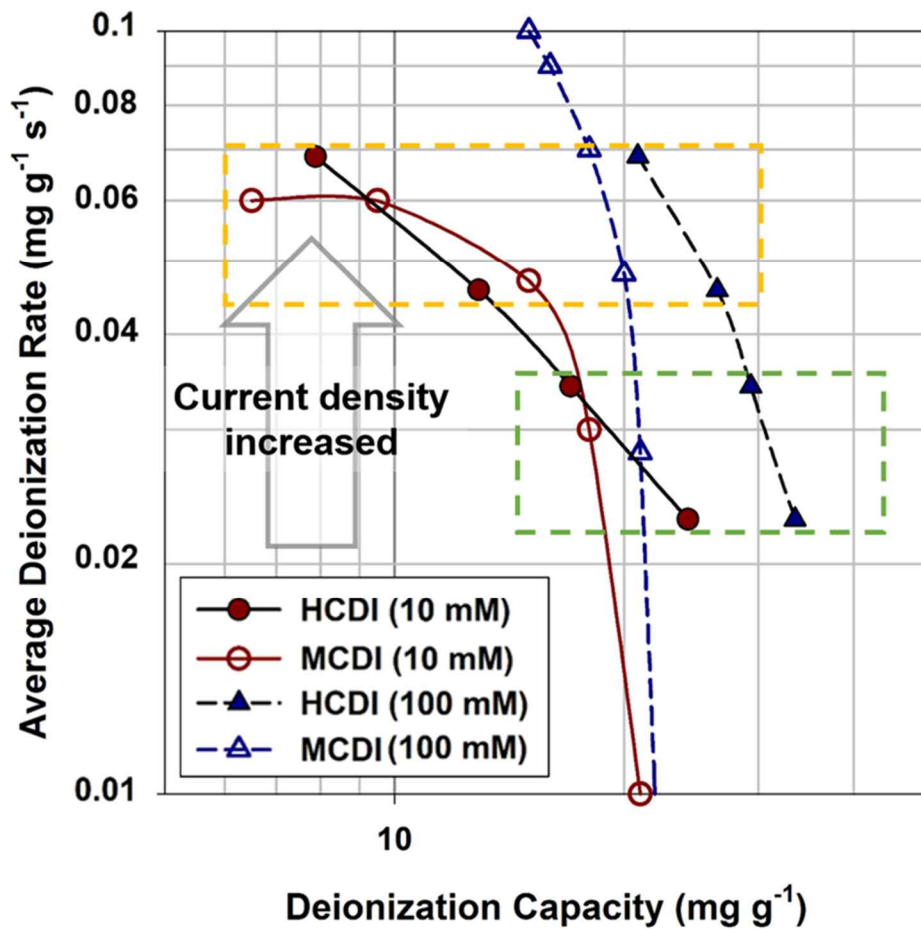
Figure 4-10. HCDI Ragone plot of $Na_2FeP_2O_7$ with respect to the influent concentration (10 mM (●—) and 100 mM (-▲-·) NaCl) and current density (1 mA cm^{-2}, 1.5 mA cm^{-2}, 2 mA cm^{-2} and 3 mA cm^{-2}), including the results in Figure 6(a). The results of MCDI at 10 mM (○—) and 100 mM (-△-) are included for comparative purposes (Kim and Yoon 2015).

97

4.4.   Summary

In this study, sodium iron pyrophosphate ($Na_2FeP_2O_7$) was successfully examined as a new material for the HCDI system, and an analysis of the CDI Ragone plot allowed for the examination of the effects of various operation parameters on the system. The HCDI system with $Na_2FeP_2O_7$ showed a superior maximum deionization rate performance (0.08 mg g^{-1} s^{-1}) with a comparable deionization capacity performance (30.2 mg g^{-1}) compared to the CDI, MCDI and even HCDI from a previous study (the system with $Na_4Mn_9O_{18}$). Furthermore, the analysis of the CDI Ragone plot revealed that the hybrid behavior characteristics, high deionization capacity that originated from the high capacity of $Na_2FeP_2O_7$ and fast deionization rates resulting from the supercapacitor depended on the operation conditions, including the current density, cell voltage and influent concentration.

5. Conclusion

In this dissertation, a novel electrochemical water treatment system and suitable materials for deionization and oxidation were successfully investigated.

First of all, a novel hybrid electrochemical water treatment system combining an electrochemical desalination system with an oxidation process was successfully demonstrated by intercalation of cations on a cathode, spontaneous diffusion of anions through the anion exchange membrane and the simultaneous reaction of chlorine generation. As a primary result, world record-level desalination capacities of approximately 87 mg g^{-1} and 36 mg g^{-1} were achieved in 35 g L^{-1} and 3 g L^{-1} NaCl, respectively. In addition, this hybrid system showed a coulombic efficiency of approximately 98% and 66% in synthetic brackish water for desalination and oxidation, respectively. The m-Blue TiO2 NT as an anode electrode functions efficiently for chlorine generation, even in low concentrations of electrolyte. Consequently, by combining the desalination process and the oxidation process, this hybrid system showed superior desalination capacity and efficiency, and it provided a new strategy to overcome the limitations of materials used for capturing anions.

Second, sodium iron pyrophosphate ($Na_2FeP_2O_7$) was successfully examined as a new material for the HCDI system, and an analysis of the CDI Ragone plot allowed for the examination of the effects of various operation parameters on the system. The HCDI system with $Na_2FeP_2O_7$ showed a superior maximum deionization rate performance (0.08 mg g^{-1} s^{-1}) with a comparable deionization capacity performance (30.2 mg g^{-1}) compared to the CDI, MCDI and even HCDI from a previous study (the system with $Na_4Mn_9O_{18}$). Furthermore, the analysis of the CDI Ragone plot revealed that the hybrid behavior characteristics, high deionization capacity that originated from the high capacity of $Na_2FeP_2O_7$ and fast deionization rates resulting from the supercapacitor depended on the operation conditions, including the current density, cell voltage and influent concentration. This HCDI system with $Na_2FeP_2O_7$ contributes to expanding the understanding for kinetic or thermodynamic properties of the HCDI system.

References

Anderson, M. A., A. L. Cudero and J. Palma (2010). "Capacitive deionization as an electrochemical means of saving energy and delivering clean water. Comparison to present desalination practices: Will it compete?" Electrochimica Acta **55**(12): 3845-3856.

Avraham, E., Y. Bouhadana, A. Soffer and D. Aurbach (2009). "Limitation of charge efficiency in capacitive deionization I. On the behavior of single activated carbon." Journal of the Electrochemical Society **156**(6): P95-P99.

Avraham, E., M. Noked, Y. Bouhadana, A. Soffer and D. Aurbach (2009). "Limitations of charge efficiency in capacitive deionization II. On the behavior of cdi cells comprising two activated carbon electrodes." Journal of the Electrochemical Society **156**(10): P157-P162.

Barbieri, O., M. Hahn, A. Herzog and R. Kötz (2005). "Capacitance limits of high surface area activated carbons for double layer capacitors." Carbon **43**(6): 1303-1310.

Bard, A. J. and L. R. Faulkner (2001). "Electrochemical methods: principles and applications." Electrochemical Methods: Principles and Applications: 386-428.

Biesheuvel, P. and A. Van der Wal (2010). "Membrane capacitive deionization." Journal of Membrane Science **346**(2): 256-262.

Biesheuvel, P., B. Van Limpt and A. Van der Wal (2009). "Dynamic adsorption/desorption process model for capacitive deionization." The Journal of Physical Chemistry C **113**(14): 5636-5640.

Brillas, E., I. Sirés and M. A. Oturan (2009). "Electro-Fenton process and related electrochemical technologies based on Fenton's reaction chemistry." Chemical Reviews **109**(12): 6570-6631.

Chen, C.-Y., K. Matsumoto, T. Nohira, R. Hagiwara, Y. Orikasa and Y. Uchimoto (2014). "Pyrophosphate $Na_2FeP_2O_7$ as a low-cost and high-performance positive electrode material for sodium secondary batteries utilizing an inorganic ionic liquid." Journal of Power Sources **246**: 783-787.

El-Deen, A. G., N. A. Barakat, K. A. Khalil and H. Y. Kim (2013). "Development of multi-channel carbon nanofibers as effective electrosorptive electrodes for a capacitive deionization process." Journal of Materials Chemistry A **1**(36): 11001-11010.

Elimelech, M. and W. A. Phillip (2011). "The future of seawater desalination: energy, technology, and the environment." science **333**(6043): 712-717.

102

Erragh, F., A. Boukhari, B. Elouadi and E. M. Holt (1991). "Crystal structures of two allotropic forms of $Na_2CoP_2O_7$." Journal of crystallographic and spectroscopic research **21**(3): 321-326.

Farmer, J. C., D. V. Fix, G. V. Mack, R. W. Pekala and J. F. Poco (1996). "Capacitive deionization of NaCl and $NaNO_3$ solutions with carbon aerogel electrodes." Journal of the Electrochemical Society **143**(1): 159-169.

Gao, X., A. Omosebi, J. Landon and K. Liu (2014). "Dependence of the capacitive deionization performance on potential of zero charge shifting of carbon xerogel electrodes during long-term operation." Journal of The Electrochemical Society **161**(12): E159-E166.

Gao, X., A. Omosebi, J. Landon and K. Liu (2015). "Enhanced salt removal in an inverted capacitive deionization cell using amine modified microporous carbon cathodes." Environmental science & technology **49**(18): 10920-10926.

Gao, X., A. Omosebi, J. Landon and K. Liu (2015). "Surface charge enhanced carbon electrodes for stable and efficient capacitive deionization using inverted adsorption–desorption behavior." Energy & Environmental Science **8**(3): 897-909.

Hoganson, C. W. and G. T. Babcock (1997). "A metalloradical mechanism for the generation of oxygen from water in photosynthesis." Science **277**(5334): 1953-1956.

Jeon, S.-i., H.-r. Park, J.-g. Yeo, S. Yang, C. H. Cho, M. H. Han and D. K. Kim (2013). "Desalination via a new membrane capacitive deionization process utilizing flow-electrodes." Energy & Environmental Science **6**(5): 1471-1475.

Jeon, S.-i., J.-g. Yeo, S. Yang, J. Choi and D. K. Kim (2014). "Ion storage and energy recovery of a flow-electrode capacitive deionization process." Journal of Materials Chemistry A **2**(18): 6378-6383.

Jeong, J., C. Kim and J. Yoon (2009). "The effect of electrode material on the generation of oxidants and microbial inactivation in the electrochemical disinfection processes." Water Research **43**(4): 895-901.

Jo, C., Y. Park, J. Jeong, K. T. Lee and J. Lee (2015). "Structural effect on electrochemical performance of ordered porous carbon electrodes for Na-ion batteries." ACS applied materials & interfaces **7**(22): 11748-11754.

Jung, Y. H., C. H. Lim, J.-H. Kim and D. K. Kim (2014). "$Na_2FeP_2O_7$ as a positive electrode material for rechargeable aqueous sodium-ion batteries." RSC ADVANCES **4**(19): 9799-9802.

Kim, C., S. Kim, J. Choi, J. Lee, J. S. Kang, Y.-E. Sung, J. Lee, W. Choi and J. Yoon (2014). "Blue TiO_2 Nanotube Array as an oxidant generating novel anode material fabricated by simple cathodic polarization." Electrochimica Acta **141**: 113-119.

Kim, C., J. Lee, S. Kim and J. Yoon (2014). "TiO_2 sol–gel spray method for carbon electrode fabrication to enhance desalination efficiency of capacitive deionization." Desalination **342**: 70-74.

Kim, H., J. Hong, K.-Y. Park, H. Kim, S.-W. Kim and K. Kang (2014). "Aqueous rechargeable Li and Na ion batteries." Chemical reviews **114**(23): 11788-11827.

Kim, H., R. Shakoor, C. Park, S. Y. Lim, J. S. Kim, Y. N. Jo, W. Cho, K. Miyasaka, R. Kahraman and Y. Jung (2013). "$Na_2FeP_2O_7$ as a promising iron‐based pyrophosphate cathode for sodium rechargeable batteries: A combined experimental and theoretical Study." Advanced Functional Materials **23**(9): 1147-1155.

Kim, S., J. Lee, J. S. Kang, K. Jo, S. Kim, Y.-E. Sung and J. Yoon (2015). "Lithium recovery from brine using a λ-MnO_2/activated carbon hybrid supercapacitor system." Chemosphere **125**: 50-56.

Kim, S., J. Lee, C. Kim and J. Yoon (2016). "$Na_2FeP_2O_7$ as a novel material for hybrid capacitive deionization." Electrochimica Acta **203**: 265-271.

Kim, T. and J. Yoon (2013). "Relationship between capacitance of activated carbon composite electrodes measured at a low electrolyte concentration and their desalination performance in capacitive deionization." Journal of Electroanalytical Chemistry **704**: 169-174.

Kim, T. and J. Yoon (2015). "CDI ragone plot as a functional tool to evaluate desalination performance in capacitive deionization." RSC Advances **5**(2): 1456-1461.

Kim, Y.-J. and J.-H. Choi (2010). "Enhanced desalination efficiency in capacitive deionization with an ion-selective membrane." Separation and Purification Technology **71**(1): 70-75.

Kuhn, A. and C. Mortimer (1972). "The efficiency of chlorine evolution in dilute brines on ruthenium dioxide electrodes." Journal of Applied Electrochemistry **2**(4): 283-287.

La Mantia, F., M. Pasta, H. D. Deshazer, B. E. Logan and Y. Cui (2011). "Batteries for efficient energy extraction from a water salinity difference." Nano letters **11**(4): 1810-1813.

Lee, J.-B., K.-K. Park, H.-M. Eum and C.-W. Lee (2006). "Desalination of a thermal power plant wastewater by membrane capacitive deionization." Desalination **196**(1): 125-134.

Lee, J., S. Kim, C. Kim and J. Yoon (2014). "Hybrid capacitive deionization to enhance the desalination performance of capacitive techniques." Energy & Environmental Science **7**(11): 3683-3689.

Lee, J., S.-H. Yu, C. Kim, Y.-E. Sung and J. Yoon (2013). "Highly selective lithium recovery from brine using a λ-MnO$_2$–Ag battery." Physical Chemistry Chemical Physics **15**(20): 7690-7695.

Li, H., S. Liang, J. Li and L. He (2013). "The capacitive deionization behaviour of a carbon nanotube and reduced graphene oxide composite." Journal of Materials Chemistry A **1**(21): 6335-6341.

Li, H., L. Pan, C. Nie, Y. Liu and Z. Sun (2012). "Reduced graphene oxide and activated carbon composites for capacitive deionization." Journal of Materials Chemistry **22**(31): 15556-15561.

Li, H., L. Zou, L. Pan and Z. Sun (2010). "Novel graphene-like electrodes for capacitive deionization." Environmental science & technology **44**(22): 8692-8697.

Li, L., L. Zou, H. Song and G. Morris (2009). "Ordered mesoporous carbons synthesized by a modified sol–gel process for electrosorptive removal of sodium chloride." Carbon **47**(3): 775-781.

Martinez-Huitle, C. A. and S. Ferro (2006). "Electrochemical oxidation of organic pollutants for the wastewater treatment: direct and indirect processes." Chemical Society Reviews **35**(12): 1324-1340.

Oren, Y. (2008). "Capacitive deionization (CDI) for desalination and water treatment—past, present and future (a review)." Desalination **228**(1): 10-29.

Pasta, M., A. Battistel and F. La Mantia (2012). "Batteries for lithium recovery from brines." Energy & Environmental Science **5**(11): 9487-9491.

Pasta, M., C. D. Wessells, Y. Cui and F. La Mantia (2012). "A desalination battery." Nano letters **12**(2): 839-843.

Porada, S., L. Borchardt, M. Oschatz, M. Bryjak, J. Atchison, K. Keesman, S. Kaskel, P. Biesheuvel and V. Presser (2013). "Direct prediction of the desalination performance of porous carbon electrodes for capacitive deionization." Energy & Environmental Science **6**(12): 3700-3712.

Porada, S., D. Weingarth, H. V. Hamelers, M. Bryjak, V. Presser and P. Biesheuvel (2014). "Carbon flow electrodes for continuous operation of capacitive deionization and capacitive mixing energy generation." Journal of Materials Chemistry A **2**(24): 9313-9321.

Porada, S., R. Zhao, A. Van Der Wal, V. Presser and P. Biesheuvel (2013). "Review on the science and technology of water desalination by capacitive deionization." Progress in Materials Science **58**(8): 1388-1442.

Qian, B., G. Wang, Z. Ling, Q. Dong, T. Wu, X. Zhang and J. Qiu (2015). "Sulfonated graphene as cation-selective coating: A new strategy for high performance membrane capacitive deionization." Advanced Materials Interfaces **2**(16).

Rajkumar, D., J.-G. Kim and K. K. Kim (2004). "A study on electrochemical, oxidation of catechol in chloride medium for wastewater treatment application." Environ. Eng. Res. **9**(6): 279-287.

Richard T. Mayes, C. T., James O. Kiggans Jr., Shannon M. Mahurin, David W. DePaoli and Sheng Dai (2010). "Hierarchical ordered mesoporous carbon from phloroglucinol-glyoxal and its application in capacitive deionization of brackish water." Journal of Materials Chemistry **20**(39): 8674-8678.

Ryoo, M.-W. and G. Seo (2003). "Improvement in capacitive deionization function of activated carbon cloth by titania modification." Water Research **37**(7): 1527-1534.

Sadrzadeh, M. and T. Mohammadi (2008). "Sea water desalination using electrodialysis." Desalination **221**(1): 440-447.

Sauvage, F., E. Baudrin and J.-M. Tarascon (2007). "Study of the potentiometric response towards sodium ions of $Na_{0.44-x}MnO_2$ for the development of selective sodium ion sensors." Sensors and Actuators B: Chemical **120**(2): 638-644.

Sauvage, F., L. Laffont, J.-M. Tarascon and E. Baudrin (2007). "Study of the insertion/deinsertion mechanism of sodium into $Na_{0.44}MnO_2$." Inorganic chemistry **46**(8): 3289-3294.

Service, R. F. (2006). "Desalination freshens up." <u>Science (New York, NY)</u> **313**(5790): 1088.

Slater, M. D., D. Kim, E. Lee and C. S. Johnson (2013). "Sodium Ion Batteries." <u>Advanced Functional Materials</u> **23**(8): 947-958.

Smith, K. C. and R. Dmello (2016). "Na-Ion desalination (NID) enabled by Na-blocking membranes and symmetric Na-intercalation: porous-electrode modeling." <u>Journal of The Electrochemical Society</u> **163**(3): A530-A539.

Sung-il Jeon, H.-r. P., Jeong-gu Yeo, SeungCheol Yang, Churl Hee Cho, Moon Hee Han and Dong Kook Kim (2013). "Desalination via a new membrane capacitive deionization process utilizing flow-electrodes." <u>Energy & Environmental Science</u> **6**(5): 1471-1475.

Suss, M., S. Porada, X. Sun, P. Biesheuvel, J. Yoon and V. Presser (2015). "Water desalination via capacitive deionization: What is it and what can we expect from it?" <u>Energy & Environmental Science</u>.

Suss, M., S. Porada, X. Sun, P. Biesheuvel, J. Yoon and V. Presser (2015). "Water desalination via capacitive deionization: what is it and what can we expect from it?" <u>Energy & Environmental Science</u> **8**(8): 2296-2319.

Suss, M. E., T. F. Baumann, W. L. Bourcier, C. M. Spadaccini, K. A. Rose, J. G. Santiago and M. Stadermann (2012). "Capacitive desalination with

flow-through electrodes." Energy & Environmental Science **5**(11): 9511-9519.

Trócoli, R., A. Battistel and F. L. Mantia (2014). "Selectivity of a lithium recovery process based on LiFePO₄." Chemistry–A European Journal **20**(32): 9888-9891.

Vörösmarty, C. J., P. B. McIntyre, M. O. Gessner, D. Dudgeon, A. Prusevich, P. Green, S. Glidden, S. E. Bunn, C. A. Sullivan and C. R. Liermann (2010). "Global threats to human water security and river biodiversity." Nature **467**(7315): 555-561.

Wang, G., Q. Dong, Z. Ling, C. Pan, C. Yu and J. Qiu (2012). "Hierarchical activated carbon nanofiber webs with tuned structure fabricated by electrospinning for capacitive deionization." Journal of Materials Chemistry **22**(41): 21819-21823.

Wang, H., L. Shi, T. Yan, J. Zhang, Q. Zhong and D. Zhang (2014). "Design of graphene-coated hollow mesoporous carbon spheres as high performance electrodes for capacitive deionization." Journal of Materials Chemistry A **2**(13): 4739-4750.

Welgemoed, T. and C. Schutte (2005). "Capacitive deionization technology™: an alternative desalination solution." Desalination **183**(1): 327-340.

111

Wimalasiri, Y. and L. Zou (2013). "Carbon nanotube/graphene composite for enhanced capacitive deionization performance." Carbon **59**: 464-471.

Xu, P., J. E. Drewes, D. Heil and G. Wang (2008). "Treatment of brackish produced water using carbon aerogel-based capacitive deionization technology." Water Research **42**(10): 2605-2617.

Xu, X., L. Pan, Y. Liu, T. Lu, Z. Sun and D. H. Chua (2015). "Facile synthesis of novel graphene sponge for high performance capacitive deionization." Scientific reports **5**.

Yang, S. J., T. Kim, K. Lee, Y. S. Kim, J. Yoon and C. R. Park (2014). "Solvent evaporation mediated preparation of hierarchically porous metal organic framework-derived carbon with controllable and accessible large-scale porosity." Carbon **71**: 294-302.

Yin, H., S. Zhao, J. Wan, H. Tang, L. Chang, L. He, H. Zhao, Y. Gao and Z. Tang (2013). "Three dimensional graphene/metal oxide nanoparticle hybrids for high performance capacitive deionization of saline water." Advanced Materials **25**(43): 6270-6276.

Zhang, D., X. Wen, L. Shi, T. Yan and J. Zhang (2012). "Enhanced capacitive deionization of graphene/mesoporous carbon composites." Nanoscale **4**(17): 5440-5446.

Zhang, D., T. Yan, L. Shi, Z. Peng, X. Wen and J. Zhang (2012). "Enhanced capacitive deionization performance of graphene/carbon nanotube composites." Journal of Materials Chemistry **22**(29): 14696-14704.

Zhao, R., P. Biesheuvel, H. Miedema, H. Bruning and A. Van der Wal (2009). "Charge efficiency: a functional tool to probe the double-layer structure inside of porous electrodes and application in the modeling of capacitive deionization." The Journal of Physical Chemistry Letters **1**(1): 205-210.

Zhao, R., O. Satpradit, H. Rijnaarts, P. Biesheuvel and A. Van der Wal (2013). "Optimization of salt adsorption rate in membrane capacitive deionization." Water research **47**(5): 1941-1952.

국문초록

최근 수십 년 동안 사용 가능한 물 부족은 인류에게 중대한 위기로써 인식되고 있다. 전기화학적 수처리 기술은 높은 에너지 효율과 친환경 적이며 유해한 화학 약품을 요구하지 않기 때문에 이러한 문제를 극복할 수 있는 대안으로 생각할 수 있다. 축전식 탈염기술, 전기투석법 및 배터리 원리를 이용한 담수화기술이 에너지 저장 소재와 전기화학적 수처리 기술이 매우 정교하게 결합된 대표적인 융합 기술들이다. 이러한 융합 기술들은 슈퍼캐퍼시터나 배터리와 같은 에너지 저장 소재에 에너지가 저장되는 기본 원리를 기반으로 전기화학적 담수화 공정을 성공적으로 완성하였다. 이러한 시스템들은 높은 에너지 효율을 달성 할 수 있는 수처리 기술을 제공하였으나, 음이온을 탈이온화 할 수 있는 시스템 및 적합한 전극 물질을 개발하는 어려움과 수계 시스템에서 활물질의 안정성을 확보하고 어렵다는 시스템 및 전극 물질 개발의 한계가 있다.

본 학위 논문에서는 탈염과 산화가 결합된 새로운 전기화학적 수처리 시스템과 양이온이 탈삽입 가능한 새로운 물질에 대한

연구를 수행하였다. 먼저, 전기화학적 산화 공정과 탈염 공정이 동시에 수행되는 새로운 전기화학적 수처리 시스템을 개발하였다. 본 시스템은 탈염 공정을 위한 소듐배터리 전극과 산화 공정을 위한 산화 전극으로 구성된다. 주요한 결과로는 35 g L^{-1} 와 3 g L^{-1} 의 염화소듐 수용액에서 각각 약 87 mg g^{-1} 과 36 mg g^{-1} 의 탈염 용량을 보였으며, 다양한 이온이 존재하는 2.79 g L^{-1} 의 모의 합성수 수준에서도 98% 의 전하효율을 탈염 공정에서 보였으며, 산화 공정의 효율도 66% 수준이었다.

다음으로 피로인산철소듐을 이용한 하이브리드 축전식 탈염 공정에 대한 연구를 수행하였다. 본 연구에서는 양이온을 탈이온화 시키는 전극으로 피로인산철소듐을 이용하여 전반적인 하이브리드 축전식 탈염 공정의 성능에 대하여 연구하였다. 주요 결과로는 기존에 보고된 하이브리드 축전식 탈염 공정과 유사한 용량을 보이지만 속도면에서 향상된 탈염 성능을 보였으며, Ragone plot 분석을 통하여 배터리와 슈퍼캐퍼시터가 결합된 하이브리드 축전식 탈염 공정의 높은 용량과 빠른 속도 특성에 대하여 규명하였다.

이러한 새로운 전기화학적 수처리 기술 및 전극 개발이 음이온 탈이온화를 위한 전극 물질 개발의 한계를 극복하고 새로운 시스템의 전기화학적 수처리 공정의 특성을 규명하는 새로운 방안을 제공하는데 기여 할 수 있을 것이다.

주요어: 하이브리드 전기화학적 수처리 시스템; 탈염 공정 및 산화 공정; 블루 타이타이나 나노튜브; 하이브리드 축전식 탈염기술; 피로인산철소듐

학번: 2010-20983